

Orbital CO₂ reconstruction using boron isotopes during the late Pleistocene, an assessment of accuracy.

Elwyn de la Vega^{ab}, Thomas B. Chalk^{ac}, Mathis P. Hain^d, Megan R. Wilding^a, Daniel Casey^a, Robin Gledhill^a, Chongguang Luo^{ac}, Paul A. Wilson^a, Gavin L. Foster^a.

^aSchool of Ocean and Earth Science, National Oceanography Centre Southampton, University of Southampton, Waterfront campus, Southampton SO14 3ZH, UK.

^bUniversity of Galway, Ollscoil na Gaillimhe, [School of Geography, Archaeology & Irish Studies](#) department of Geography, University Road, Galway, H91 TK33, Ireland.

^c[Aix Marseille Université, CNRS, IRD, INRAE, CEREGE, Aix-en-Provence, France](#) ^e[Centre Européen de Recherche et d'Enseignement des Géosciences de l'Environnement \(CEREGE\), Bâtiment Pasteur, Europole Méditerranéen de l'Arbois BP80, 13545 Aix-en-Provence cedex 4.](#)

^dEarth and Planetary Sciences, University of California, Santa Cruz, CA, USA.

^eState Key Laboratory of Ore Deposit Geochemistry, Institute of Geochemistry, Chinese Academy of Sciences, Guiyang 550081, P.R. China.

Correspondence to Elwyn de la Vega: elwyn.delavega@universityofgalway.ie

Abstract.

Boron isotopes in planktonic foraminifera are a widely used proxy to determine ancient surface seawater pH, and by extension atmospheric CO₂ concentration and climate forcing on geological time scales. Yet, to reconstruct absolute values for pH and CO₂, we require a $\delta^{11}\text{B}_{\text{foram-borate}}$ to pH calibration and independent determinations of ocean temperature, salinity, a second carbonate parameter, and the boron isotope composition of seawater. Although $\delta^{11}\text{B}$ -derived records of atmospheric CO₂ have been shown to perform well against ice core-based CO₂ reconstructions, these tests have been performed at only a few locations and with limited temporal resolution. Here we present two highly resolved CO₂ records for the late Pleistocene from ODP Sites 999 and 871. Our $\delta^{11}\text{B}$ -derived CO₂ record shows a very good agreement with the ice core CO₂ record with an average offset of 13 ± 46 (2σ) -4.6 ± 49 (2σ) ppm, and a RMSE of 26 ~~25~~ ppm, with minor short-lived overestimations of CO₂ (of up to ~50 ppm) occurring during some glacial onsets. We explore potential drivers of this disagreement and conclude that partial dissolution of foraminifera has a minimal effect on the CO₂ offset. We also observe that the general agreement between $\delta^{11}\text{B}$ -derived and ice core CO₂ is improved by optimising the $\delta^{11}\text{B}_{\text{foram-borate}}$ calibration. Despite these minor issues a strong linear relationship between relative change in climate forcing from CO₂ (from ice core data) and pH change (from $\delta^{11}\text{B}$) exists over the late Pleistocene, confirming that pH change is a robust proxy of climate forcing over relatively short (<1 million year) intervals. Overall, these findings demonstrate that the boron isotope proxy is a reliable indicator of CO₂ beyond the reach of the ice cores and can help improve determinations of climate sensitivity for ancient time intervals.

1- Introduction.

The boron isotope composition of ancient planktonic foraminifera shells is widely used to reconstruct past concentrations of atmospheric CO₂ to understand the drivers and responses of climate change over orbital and geological time scales. Unlike many environmental proxies where it is difficult to assess the accuracy of the resulting reconstructions (e.g. for sea surface temperature), the boron isotope pH/CO₂ proxy can directly be compared with the ice core CO₂ records, i.e. the West Antarctic ice sheet divide (Ahn et al., 2012), the EPICA (European Project for Ice Coring in Antarctica) dome Concordia ice core record (Siegenthaler et al., 2005; Lüthi et al., 2008; Bereiter et al., 2015), and the Vostock ice core

45 record (Petit et al., 1999). This comparison of CO₂ over the last 800 kyr provides a very powerful test
 46 of proxy accuracy. Several past intervals have been studied to test the boron isotope proxy in this way
 47 (Sanyal et al., 1995; Foster, 2008; Hönisch and Hemming, 2005; Henehan et al., 2013; Raitzsch et al.,
 48 2018).

49 Given the success of these comparisons, the boron isotope proxy has been used to investigate the
 50 interaction between CO₂, the ocean carbon cycle and climate beyond the reach of the ice cores, such as
 51 during the Mid-Pleistocene transition (Hönisch et al., 2009; Chalk et al., 2017; Dyez et al., 2018), the
 52 Pliocene (Martinez-Boti et al., 2015, de la Vega et al., 2020), the Miocene (Foster et al., 2012; Greenop
 53 et al., 2014, Guillermic et al., 2022), the Eocene (Anagnostou et al., 2016, 2020; Harper et al., 2020),
 54 Paleocene-Eocene boundary (Penman et al., 2014; Gutjahr et al. 2017) and the Cretaceous-Palaeogene
 55 boundary (Henehan et al., 2019). Application of the boron isotope proxy is however complicated by the
 56 need for: (i) an empirical species-specific calibration of $\delta^{11}\text{B}_{\text{foraminifera}}$ to $\delta^{11}\text{B}_{\text{borate}}$ in the pH expression
 57 (Henehan et al., 2013, 2016, hereafter $\delta^{11}\text{B}_{\text{foram-borate}}$ calibration), sometimes including extinct species
 58 for deep-time reconstruction; (ii) $\delta^{11}\text{B}$ of seawater ($\delta^{11}\text{B}_{\text{sw}}$), temperature and salinity in the past to
 59 calculate pH from $\delta^{11}\text{B}$; and (iii) a second carbonate parameter (typically total alkalinity, ~~total~~-dissolved
 60 inorganic carbon, DIC, or calcite saturation state) to convert pH to CO₂. While these variables do not
 61 influence the magnitude of uncertainty equally in all time intervals, assessment of the boron-based
 62 reconstructions against existing ice-core records is a powerful test of the proxy's accuracy.
 63

64 Recently, Hain et al. (2018) suggested that the radiative forcing from CO₂ change (ΔF_{CO_2}) is linearly
 65 related to pH change (ΔpH) of equilibrated water of the low-latitude surface ocean when the CO₂ change
 66 occurs faster than the residence time of carbon with respect to silicate weathering (e.g., ~1 million years
 67 (Myr)). That is, glacial/interglacial CO₂ climate forcing could be estimated directly from reconstructed
 68 ΔpH . Given that one of the main priorities for accurate reconstructions of past CO₂ levels is to allow
 69 determinations of climate sensitivity, defined as the temperature response to a radiative forcing –
 70 typically a doubling of CO₂ with associated slow and fast feedbacks (e.g. Rohling et al., 2013, 2018) –
 71 this recognition may provide a useful shortcut. Climate forcing is a perturbation of the planet's energy
 72 balance averaged over the planet (Hansen et al., 2008) and CO₂ forcing, ΔF_{CO_2} expressed in $\text{W}\cdot\text{m}^{-2}$, at a
 73 given time can be written as:

$$74 \quad \Delta F_{\text{CO}_2} \cong \alpha_{2\times\text{CO}_2} * \frac{\Delta \log_{10} \text{CO}_2}{\log_{10} 2} \quad (1)$$

75 where $\alpha_{2\times\text{CO}_2}$ is the sensitivity of the radiative balance per doubling of CO₂, and $\Delta \log_{10} \text{CO}_2$ is the CO₂
 76 change over time expressed in terms of how many 10-foldings of proportional (not absolute) CO₂
 77 change (Hain et al., 2018).
 78

79 By considering basic equilibrium reactions of carbon species, $\Delta \log_{10} \text{CO}_2$ can be derived and expressed
 80 as:

$$82 \quad \Delta \log_{10} \text{CO}_2 \cong \Delta \log_{10} \text{DIC} + \Delta \text{p}K_0 + \Delta \text{p}K_1 - \Delta \text{pH} \quad (2)$$

84 Hain et al. (2018) showed that the terms $\Delta \log_{10} \text{DIC}$ and $\Delta \text{p}K_0 + \Delta \text{p}K_1$ are small and that $\Delta \log_{10} \text{CO}_2$ can
 85 therefore simply be expressed as :

$$87 \quad \Delta \log_{10} \text{CO}_2 \cong -\Delta \text{pH} \quad (3a)$$

$$89 \quad \Delta F_{\text{CO}_2} \cong -\frac{\log_{10} 2}{\alpha_{2\times\text{CO}_2}} \Delta \text{pH} \cong -12.3 \Delta \text{pH} \quad (3b)$$

91 To assess the uncertainty of this approximate -1:1 $\Delta \log_{10} \text{CO}_2 / \Delta \text{pH}$ relationship Hain et al. (2018)
 92 considered three different end-member causes to compute the accurate $\Delta \log_{10} \text{CO}_2 / \Delta \text{pH}$ relationship:
 93 (1) DIC addition/removal yields a slope of -1.3:1 (relative to the basic formalism), (2) CaCO₃
 94 addition/removal (e.g. precipitation/dissolution, riverine input) yields a slope of -0.9:1, and (3)

95 warming/cooling yields a slope of -1.1:1. That is, even if ΔpH was known exactly this range of
96 plausible slopes results in estimated $\Delta\log_{10}\text{CO}_2$ and ΔF_{CO_2} that are systematically biased by -10% for
97 change caused purely by CaCO_3 variations or +30% for change purely caused by DIC variations
98 relative to the approximate -1:1 $\Delta\log_{10}\text{CO}_2/\Delta\text{pH}$ relationship. While introducing such structural
99 uncertainty in the estimation of ΔF_{CO_2} is a concern, this approach eliminates the need to assume a
100 second carbonate system parameter and the uncertainty incurred thereby. An estimate of $\delta^{11}\text{B}_{\text{sw}}$ is still
101 needed to reconstruct pH based on the boron isotope proxy system (Foster and Rae, 2016) but
102 estimated pH change (i.e., ΔpH) is much less sensitive to error in assumed $\delta^{11}\text{B}_{\text{sw}}$ than is absolute pH
103 (Hain et al., 2018). An important caveat to estimating ΔF_{CO_2} directly from ΔpH is that the intercept of
104 the $\Delta\log_{10}\text{CO}_2/\Delta\text{pH}$ relationship can change with silicate weathering carbon cycle dynamics thought
105 to be important on a ~~million-year~~million-year timescale, such that the approach is applicable for
106 orbital timescale variability and short-term shifts but not for long-term trends in ΔF_{CO_2} . Therefore, the
107 orbital timescale ice age cycles of atmospheric CO_2 reconstructed from air occluded in Antarctic ice
108 cores offer a unique opportunity to determine the $\Delta\log_{10}\text{CO}_2/\Delta\text{pH}$ relationship observationally and
109 compare to theory. ~~Furthermore, Hain et al., (2018) raise the possibility that the $\Delta\log_{10}\text{CO}_2/\Delta\text{pH}$~~
110 ~~relationship could be decomposed based on the different end-member slopes to constrain the relative~~
111 ~~importance of the mechanism causing the pH and CO_2 changes. Furthermore, given the principal~~
112 ~~drivers of the glacial-interglacial CO_2 cycles (e.g. change in water mass, sea-ice cover, the soft tissue~~
113 ~~pump, the solubility pump, the CaCO_3 counter pump and the disequilibrium pump; see Sigman et al.,~~
114 ~~2010; Hain et al., 2010, 2014 for a full review), will impact the $\Delta\log_{10}\text{CO}_2/\Delta\text{pH}$ relationship in~~
115 ~~different ways, comparing the slope of the regressed $\Delta F/\Delta\text{pH}$ line from data to theoretical~~
116 ~~endmembers (temperature, DIC, CaCO_3) could allow the primary controlling mechanisms during~~
117 ~~Glacial-Interglacial (G-IG) cycles to be deciphered.~~

118
119 In light of these recent advances, our aims here are twofold. First, we extend previous ice-core validation
120 studies (Foster, 2008; Henehan et al. 2013; Chalk et al., 2017) and test the extent to which boron
121 isotopes reconstruct CO_2 faithfully when current methods and assumptions are applied. In contrast to
122 most previous studies, we use two deep ocean sites and present $\delta^{11}\text{B}$ and CO_2 data at high temporal
123 resolution (1 sample every ~ 3 to 6 kyr). This enables: (i) a thorough test of the assumptions typically
124 made including the central tenet of atmospheric CO_2 proxies that surface ocean CO_2 remains in
125 equilibrium with the atmosphere over time at any given site, (ii) an evaluation of the overall uncertainty
126 of the proxy; (iii) an evaluation of the influence of variable foraminiferal preservation on the accuracy
127 of the CO_2 reconstructed; and (iv) a refinement of a number of the input assumptions and uncertainties,
128 including the $\delta^{11}\text{B}_{\text{borate-foram}}$ calibration. Second, we evaluate the approach of Hain et al. (2018) and
129 assess the robustness of pH change to not only provide insights into the magnitude of climate forcing
130 from CO_2 change, but also the ability of this approach to provide insights into the causes of CO_2 change
131 over glacial-interglacial cycles.

132 2. Methods.

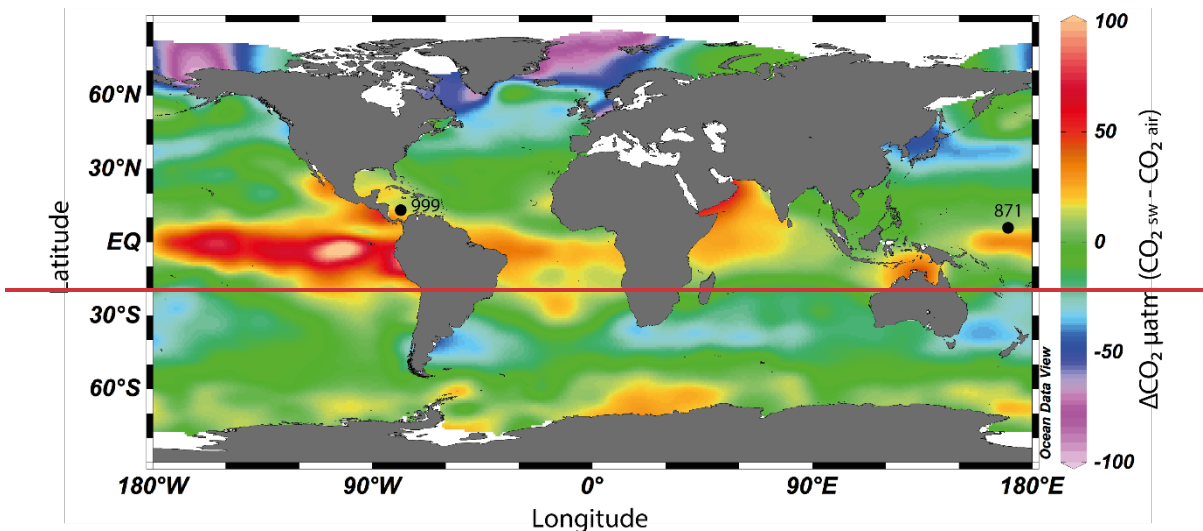
133 2.1 Core location and oceanographic setting.

134 To accurately reconstruct atmospheric CO_2 with the $\delta^{11}\text{B}\text{-CO}_2$ proxy, it is essential to measure $\delta^{11}\text{B}$ in
135 foraminifera from locations where the CO_2 flux between the ocean and the atmosphere is in near
136 equilibrium. We therefore target regions of the ocean where the water column is stratified and
137 oligotrophic as these regions are most likely to attain this condition (Takahashi et al., 2009). Here,
138 following previous studies (Foster, 2008, Henehan et al., 2013; Chalk et al., 2017), we report ~~and add~~
139 ~~new~~-data from ODP Site 999 (Figure 1, 12.75°N, 78.73°W, water depth 2827 m, sedimentation rate 3.7
140 cm/ky) in the Caribbean and supplement this well studied site with samples from ODP Site 871 in the
141 Western Pacific (5.55°N, 172.35°E, water depth 1255m, sedimentation rate ~ 1 cm/ky). The sediments
142 studied at ODP Site 871 are shallowly buried and the site today features a deep thermocline and is
143 located off the equator, hence they are unlikely to be influenced by significant equatorial upwelling

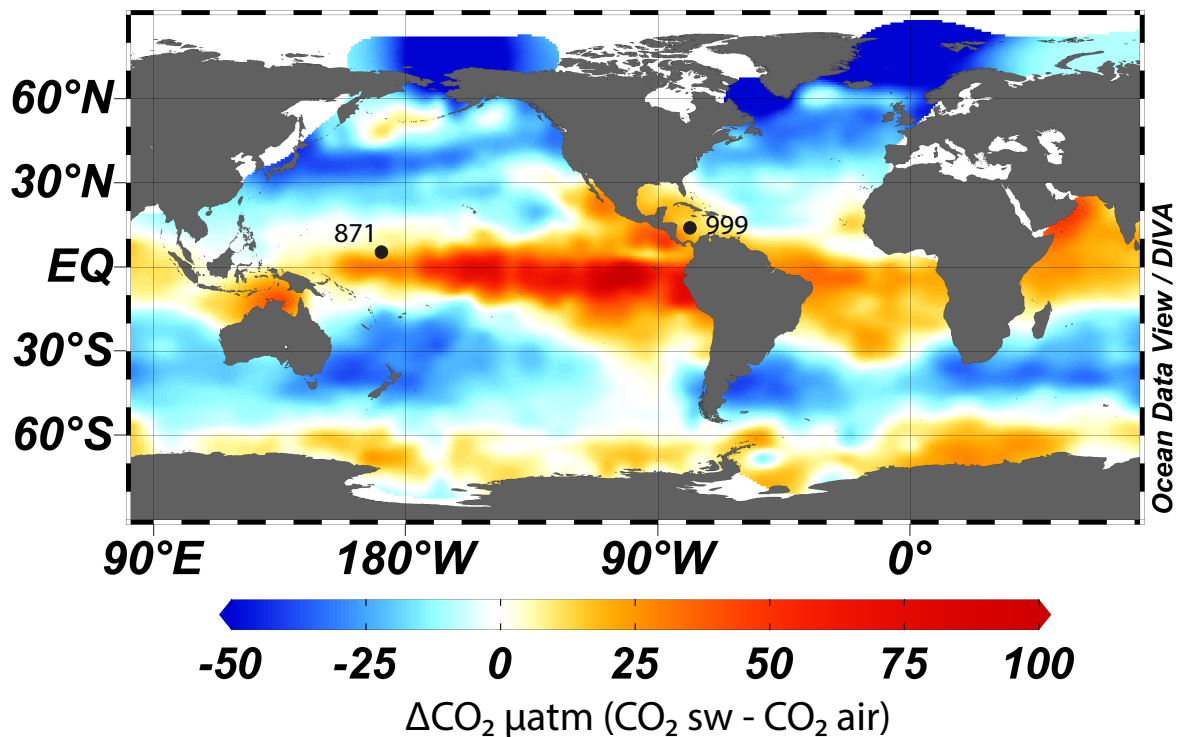
144 (Dyez and Ravelo, 2013, 2014). These two sites show a minor annual mean disequilibrium of +12 ppm
145 (range ~0 to ~30 ppm, Takahashi et al., 2009) for ODP Site 871, and +21 ppm (Olsen et al., 2004;
146 Foster, 2008) for ODP Site 999. These disequilibria are used to correct our CO₂ data derived from $\delta^{11}\text{B}$
147 and are assumed to be constant throughout the entire record presented here (with an uncertainty of ± 10
148 ppm).

149 Whilst we recognised that both sites have a minor disequilibrium, this is often a necessary
150 compromise as areas of the ocean that are in strict equilibrium with the atmosphere are often located
151 in the middle of oceanic gyres and tend to have deep sediments located under the lysocline, have a
152 low sedimentation rate and/or are outside the preferred geographic habitat of *G. ruber*. Furthermore,
153 we present surface $\delta^{18}\text{O}$ and $\delta^{13}\text{C}$ (site 871) and temperature (both sites) from *G. ruber* that provide
154 insight into the potential influence of upwelling (see section 4.2.2) at these locations. Recent Earth
155 System Model (IPSL-CM5A-MR) outputs (Gray and Evans, 2019) also show that relative pH
156 difference at our core sites between the last glacial maximum (LGM) and the pre-industrial (PI),
157 compared to the ocean average pH difference are close to 0, giving confidence that changes in local
158 disequilibrium are unlikely to drive large changes in our CO₂ reconstructions (at least during the last
159 glacial period).

160
161
162



163
164
165



166
167
168
169
170

Figure 1. Map of air-sea CO₂ disequilibrium (seawater – air) in ppm and location of ODP sites used in this study. CO₂ data from Takahashi et al. (2009). The map was made with Ocean Data View (Schlitzer, 2022).

171 **2.2 Samples.**

172 *2.2.1 Sample selection and preparation.*

173 Samples of deep-sea sediment from our two study sites were taken at 6cm (~3ky) and 10cm (~6ky)
174 resolution at ODP 871 and 999 respectively. Around 1-2 mg of the foraminifer (between 120 and 200
175 individuals) from the species *Globigerinoides ruber sensu stricto white* (here after *G. ruber ss*) were
176 hand-picked from the size fraction 300-355 μm for a target of 10 to 20 ng of boron. *G. ruber ss* was
177 chosen here because it is readily identified, is abundant throughout our chosen time interval and a
178 $\delta^{11}\text{B}_{\text{foram-borate}}$ calibration that accounts for vital effects is available from culture, plankton tows and core-
179 top samples (Henehan et al., 2013). It is also known to live in the upper surface of the ocean with a
180 relatively small depth range (Rebotim et al., 2017) which prevents significant influence of deeper more
181 remineralised CO₂-rich waters on the measured $\delta^{11}\text{B}$. The morphotype *G. ruber sensu lato* (hereafter
182 *G. ruber sl*) has slightly different morphology (Aurahs et al, 2001; Carter et al., 2017) and is thought to
183 live in deeper water compared to *G. ruber ss* (Wang, 2000). The morphotype *G. ruber sl* was also hand
184 separated and analysed at lower resolution at ODP 871 to monitor any change over time in morphotype
185 differences in $\delta^{11}\text{B}$ that could result from different habitats. For similar reasons, carbon and oxygen
186 isotopes ($\delta^{18}\text{O}$ and $\delta^{13}\text{C}$) were also measured on *G. ruber ss* and *sl* for comparison on the whole record
187 at ODP 871. For this, around 10 individuals of *G. ruber* per sample were picked, their shells gently
188 broken open and mixed and then a 100 μg aliquot of the homogenised carbonate was measured using a
189 Thermo KIEL IV Carbonate device at the University of Southampton, Waterfront Campus. While this
190 number of specimens is lower than classically done for $\delta^{18}\text{O}$ and $\delta^{13}\text{C}$ analysis, it provides power for
191 the identification of species-specific preferential diagenetic alteration, which may have occurred in the
192 sediment and it was sometimes necessary due to the scarcity of some of the *G. ruber* spp morphotypes.

193
194

195 2.2.2 Age constraints.

196 Samples were taken from 1.5 to 5 metres below sea floor (mbsf) for ODP 871 and from 9 to 21 mbsf
197 for ODP 999. Sample age at Site 871 was initially determined from sample depth using published age
198 models (Dyez and Ravelo, 2013). At Site 999, the age was determined by developing a new
199 ~~benthic~~*Cibicidoides wuellerstorfi* benthic $\delta^{18}\text{O}$ record. The initial age model at Site 871 was refined
200 by measuring $\delta^{18}\text{O}$ on the benthic species ~~*Cibicoides wuellerstorfi*~~*Uvigerina peregrina* (50 μg of 3-5
201 mixed, crushed and homogenised specimens) measured on a Thermo KIEL IV Carbonate device at
202 the University of Southampton, Waterfront Campus. These new $\delta^{18}\text{O}$ data (Figure 2) were then tuned
203 to the benthic $\delta^{18}\text{O}$ LR04 stack (Lisiecki and Raymo, 2005) using Analyseries (Paillard et al., 1996).
204 A correction of +0.47 was applied to the $\delta^{18}\text{O}$ *Cibicidoides wuellerstorfi* at ODP Site 999 following
205 Marchitto et al. (2014).

206
207

208 2.2.3 Fragment counts.

209 Foraminifera fragment counts were conducted on ODP Site 871 to monitor variations in carbonate
210 preservation. Samples were sub-sampled using a splitter (in order to maintain homogeneity) and poured
211 onto a picking tray. The fragmentation index (FI) was calculated following the approach of Howard and
212 Prell (1994) and Berger (1970) where percentage fragment is defined as:

213
214
$$FI = 100 * \frac{\text{number of fragments}}{\text{number of fragments} + \text{number of whole tests}} \quad (4)$$

215
216 Counts of whole intact grains and fragments of grains were conducted three times and averaged. The
217 standard deviation (1σ) of the fragmentation index is 1.69. This approach followed that used in an early
218 study at ODP Site 999 (Schmidt et al. 2006) ensuring that the datasets between the two sites are
219 comparable.

220 2.2.4 Boron separation.

221 The hand separated foraminifera tests for boron isotope analysis were broken open, detrital clay was
222 removed, and oxidatively cleaned and leached in a weak-acid to obtain a primary carbonate signal
223 using established methods (Barker et al., 2003). Samples were then slowly dissolved in $\sim 100 \mu\text{l}$
224 0.5M HNO_3 added to $200 \mu\text{l}$ of MQ water. Dissolved samples were then centrifuged for 5 minutes to
225 separate any remaining undissolved contaminants (e.g. silicate grains, pyrite crystals) and transferred
226 to screw top 5 ml Teflon pots for subsequent boron separation. An aliquot equivalent to 7% of each
227 sample was kept for elemental analysis and transferred to acid cleaned plastic vials in $130 \mu\text{l}$ 0.5M
228 HNO_3 . Samples were purified for boron using anion exchange column chemistry method prior to
229 isotope analysis as described elsewhere (Foster, 2008). A total procedure blank (TPB) was conducted
230 for each batch of samples and typically ranged from 0-~~100 pg~~ 50 pg which represents a blank
231 contribution of up to 2.3% (for samples containing $\sim 10\text{-}20 \text{ ng}$ of boron). Most samples had a TPB
232 below 40 pg and were not corrected. Two batches had a TPB of 70 and 100 pg for which we
233 corrected using a long-term median TPB $\delta^{11}\text{B}$ value of -7.27‰ from the University of Southampton.
234 This represents a $\delta^{11}\text{B}$ correction of 0.1 to 0.7 ‰.

235 ~~-a very small contribution relative to our sample size (0-0.25%), hence no samples required correction~~
236 ~~in this study.~~

2.3 Effect of dissolution (leaching experiment).

To investigate the effect of partial dissolution on measured $\delta^{11}\text{B}$, a leaching experiment was conducted on two species of commonly analysed planktic foraminifera: *G. ruber ss* and *Trilobatus sacculifer* (hereafter *T. sacculifer*). Around ~180 *G. ruber ss* (size 300–355 μm) and 40 *T. sacculifer* (size 500–600 μm) were picked four times and the samples were treated like so: one split was the control and received no treatment, and the three other samples (whole foraminifera) were placed in 0.0001 M Teflon distilled HNO_3 (pH 4) for 2, 4, and 6 hours respectively. The experiment was repeated for *G. ruber ss* by longer treatments, up to 10 hours in the dilute acid. The foraminifera subjected to these partial dissolution tests were then treated using the same cleaning and chromatography protocols described above.

We acknowledge that our leaching tests aren't as thorough as those described in some other studies (e.g. Brown and Elderfield, 1996; Sadekov et al., 2010) but provide useful first order insights into the susceptibility of $\delta^{11}\text{B}$ to partial dissolution of foraminiferal tests.

2.42.3 Analytical techniques

Boron isotope analyses were performed on a ThermoScientific Neptune multi collector inductively coupled plasma mass spectrometer (MC-ICPMS) with 10^{12} ΩW amplifier resistors using a standard-sample bracketing routine with NIST 951 boric acid standard (following Foster et al. 2013 and Foster, 2008). Elemental analysis was performed on each dissolved sample using a ThermoScientific Element inductively coupled plasma mass spectrometer (ICPMS). All analyses were carried out at the University of Southampton, Waterfront Campus (following Foster, 2008 and Henehan et al., 2015). Element to calcium ratios were measured with ^{43}Ca and ^{48}Ca and measured against in house mixed element standards. Elemental ratios measured included: B/Ca, Mg/Ca, Al/Ca, Mn/Ca, Sr/Ca. Based on the reproducibility of our in-house standards, the uncertainty for most elemental ratios is ~ 5% (at 95% confidence).

2.52.4 Constraints on $\delta^{11}\text{B}$ -derived pH and CO_2 .

2.5.1 From $\delta^{11}\text{B}$ to pH.

Seawater pH is related to the boron isotopic composition of dissolved borate ion by the following equation:

$$\text{pH} = \text{p}K_B - \log \left(- \frac{\delta^{11}\text{B}_{\text{sw}} - \delta^{11}\text{B}_{\text{borate}}}{\delta^{11}\text{B}_{\text{sw}} - \alpha_B \delta^{11}\text{B}_{\text{borate}} (\alpha_B - 1)} \right) \quad (5)$$

where the isotopic fractionation factor α_B between $\text{B}(\text{OH})_3$ and $\text{B}(\text{OH})_4^-$, is 1.0272 as determined by Klochko et al. (2006) and the $\delta^{11}\text{B}$ of seawater is 39.61 ‰ (Foster et al., 2010) for both sites and kept constant throughout the record due to the long residence time of boron (10–20 Myrs, Lemarchand et al. 2002).

The sea surface temperature (SST) values necessary to calculate $\text{p}K_B$ in equation (5) were determined at both sites using the Mg/Ca of *G. ruber* (Dyez and Ravelo, 2013) including a depth-dependent dissolution correction for each site (following Dyez and Ravelo, 2013 for Site 871 and Schmidt et al., 2006 for Site 999) and a pH correction using the iterative approach of Gray and Evans (2019) to account for the observed pH effect on Mg/Ca in *G. ruber* producing higher apparent sensitivity of Mg/Ca during glacial cycles (Gray et al., 2018).

Mg/Ca was corrected for depth-dependent dissolution at Site 871 using the following equation (Dyez and Ravelo, 2013):

283
$$\frac{\text{Mg}}{\text{Ca}} (\text{corrected}) = \frac{\text{Mg}}{\text{Ca}} (\text{measured}) + 0.26 * \text{depth} + 0.52_{(6a)}$$

284 Mg/Ca from Site 999 was corrected following Schmidt et al. (2006):

285
$$\frac{\text{Mg}}{\text{Ca}} (\text{corrected}) = \frac{\text{Mg}}{\text{Ca}} (\text{measured}) + 0.66_{(6b)}$$

286

287 To evaluate the effect of various Mg/Ca treatment on temperature and calculated CO₂, we performed
 288 seven sensitivity tests (Table S1) with Mg/Ca-derived SST using the calibrations of: (1) Gray et al.
 289 (2018) temperature-dependent only (global calibration), (2) Gray and Evans (2019) with a pH
 290 correction; (3) Gray et al. (2018) temperature-dependent with Mg/Ca corrected for depth-dependent
 291 dissolution; (4) Gray and Evans (2019) with Mg/Ca corrected for depth-dependent dissolution and pH
 292 correction; (5,6) Anand et al. (2003) with and without a depth correction; and (6) with temperature
 293 kept constant (26°C).

294 The differences in SST and resulting CO₂ can be substantial (Figure S1, Table S2): up to 6 degrees
 295 and ~50 ppm, respectively, between the Gray et al. (2018) calibration uncorrected for pH and the
 296 Anand et al. (2003) calibration corrected for dissolution. We have chosen the Mg/Ca treatments that
 297 accounts for pH effect on Mg/Ca and yields the closest agreement between coretop at both sites and
 298 modern temperature from Glodap v2 (Lauvset et al., 2022) This treatment is with a pH correction and
 299 Mg/Ca corrected for depth dependent dissolution. Choosing this approach is justified considering (1)
 300 the strong offset between Anand et al. (2003) multi-species Mg/Ca-Temperature calibration and the
 301 more recent *G. ruber* compilation of Gray et al., (2018); (2) the effect of pH correction as shown in
 302 Gray et al., (2018) and Gray and Evans (2019); (3) the suggested influence of dissolution on Mg/Ca
 303 (Dyez and Ravelo, 2013; Schmidt et al., 2006) and (4) the better agreement between coretop and
 304 modern SST at each site when using a pH and depth correction (Figure S1).

305

306

307

308

309 ~~the relationship of Anand et al. (2003):~~

310

311
$$SST = \frac{\ln\left(\frac{\text{Mg}_{surf}}{\text{Ca}}\right)}{0.38(\pm 0.02)} - \frac{0.09(\pm 0.003)}{0.09(\pm 0.003)} \quad (6)$$

312

313 ~~This calibration does not include a depth correction but yields temperatures from core top samples that~~
 314 ~~are consistent with modern SST (Olsen et al., 2016).~~

315 The salinity (S) that is used in the expression of pK_B is kept constant for both sites (35-PSU) due to the
 316 very minor effect of salinity on calculated pH/CO₂ (1 salinity unit changes pH by 0.006). CO₂

317

318 ~~To investigate the effect of the recently proposed pH effect on reconstructed Mg/Ca-derived SST and~~
 319 ~~hence reconstructed CO₂, we've explored a scenario wherein we apply a pH correction on Mg/Ca SST~~
 320 ~~using the iterative approach of Gray and Evans (2019).~~

321 2.5.2 From pH to CO₂.

322 Calculating CO₂ from boron isotope derived pH is dependent on the determination of a second
 323 parameter of the carbonate system. Here we use the modern value of total alkalinity (TA) at each site:
 324 2279 and 2350 μmol/kg at ODP 871 and ODP 999, respectively (Shipboard Scientific Party, 1993;

325 Takahashi et al., 2009). Following Chalk et al. (2017), these values were kept constant throughout the
 326 whole record. To account for any variations in alkalinity, a generous uniform (~~or flat~~, i.e. equal likelihood
 327 of values within the range of uncertainty) uncertainty of 175 $\mu\text{mol/kg}$, ~~-distributed equally on either side~~
 328 of the central value, is applied. (~~i.e. equal likelihood of values within the range of uncertainty~~). This
 329 range in TA encompasses the likely range in this variable on glacial-interglacial (e.g. Toggweiler, 1999;
 330 Hain et al., 2010; Cartapanis et al., 2018) or longer timescales (Hönisch et al. 2009), and its adoption
 331 means the local TA record, ~~local site~~ is not tied to a global sea-level record as ~~has~~ been practiced
 332 previously. We avoid drawing this link because the $\sim+3\%$ ($+68\mu\text{mol/kg}$) concentration increase of
 333 solute alkalinity occurring from sea-level lowering during the last glacial maximum may not have been
 334 the dominant driver of ocean alkalinity change (Boyle, 1988a/b; Sigman et al., 1998; Toggweiler, 1999;
 335 Hain et al., 2010; Cartapanis et al., 2018). By assuming a uniform distribution for TA we avoid imposing
 336 a temporal evolution to this variable because evolution of TA through a glacial cycle is uncertain and
 337 is unlikely to be simply a function of sea-level or salinity (e.g. Dyez et al. 2018) due to the effect of
 338 carbonate compensation.

339 The surface water CO_2 is then calculated as (Zeebe and Wolf-Gladrow, 2001):

340
341

$$342 \quad \text{CO}_2 = \frac{\text{TA} - \frac{K_B \cdot B_T}{K_B + [\text{H}^+]} - \frac{K_W}{[\text{H}^+]} + [\text{H}^+]}{\frac{K_1}{[\text{H}^+]} + \frac{2K_1 K_2}{[\text{H}^+]^2}} \quad (7)$$

343

344 where TA is the total alkalinity, K_B the equilibrium constant of boron species in seawater, B_T the
 345 concentration of boron in seawater (432.6 $\mu\text{mol/kg}$, Lee et al., 2010), $[\text{H}^+]$ the concentration of H^+
 346 determined from $\text{pH} = -\log [\text{H}^+]$, K_W the dissociation constant of water (function of T, S and pressure),
 347 K_1 and K_2 the first and second dissociation constants of carbonic acid (function of T, S and pressure,
 348 Luecker et al., 2000). The estimate of atmospheric CO_2 includes site-specific offsets relative to
 349 reconstructed surface water CO_2 to account for observed local disequilibrium (+21 ppm and +12 ppm
 350 at ODP Sites 999 and 871, respectively).

351 2.6 Uncertainty.

352 2.6.1 Analytical uncertainty.

353 The uncertainty on the measured $\delta^{11}\text{B}$ is expressed as the external uncertainty which includes
 354 instrumental error and chemical separation of the sample (see a detailed discussion in John and Adkins,
 355 2010). This was determined empirically by long-term repeat measurements of JCp-1 subject to the same
 356 chemical purification as our foraminiferal samples. As discussed by Rae et al. (2011) this uncertainty
 357 is dependent on the intensity of the ^{11}B signal and is expressed here by the following relationship defined
 358 during the duration of this study at the University of Southampton (Anagnostou et al., 2019), for ^{11}B
 359 intensities $<0.54\text{V}$:

$$360 \quad 2\sigma = 129600 e^{-212 \times [^{11}\text{B}]} + 0.3385 e^{-1.544 \times [^{11}\text{B}]} \quad (8).$$

361

362 where $[^{11}\text{B}]$ is the intensity of ^{11}B signal in volts. The $\delta^{11}\text{B}$ uncertainty for ^{11}B intensities $> 0.54\text{V}$ is
 363 0.15‰ (at 95% confidence).

364 2.6.2 pH and CO_2 uncertainty.

365 The CO_2 uncertainty we report was calculated with a Monte Carlo simulation (10, 000 realisations) in
 366 order to fully account for the uncertainty in all variables used in the calculation of pH and CO_2 (σ_{CO_2}
 367 $\delta^{11}\text{B}$ -derived). The shape of the uncertainty distribution sampled is either normally distributed (for
 368 temperature, salinity and $\delta^{11}\text{B}$) or uniform (for alkalinity, as discussed above). The maximum

369 probability of all realisations was used as the central value for CO₂ and an error envelope at 1 and 2σ
370 was calculated based on the 68% and 95-% distribution of the realisations.
371

372 2.6.3 Uncertainty on the CO₂ offset

373 To constrain the offset between δ¹¹B-derived CO₂ and ice core CO₂, each sediment age is compared to
374 the ice core CO₂ record by interpolation of the record of highest resolution (in this case the δ¹¹B record
375 onto the ice core compilation). To fully account for age uncertainty when interpolating the sediment
376 age to the well-dated ice core record, a distribution of the ice core data was calculated within the 4σ
377 uncertainty of the δ¹¹B age and weighed by the respective likelihood based on the age difference
378 between ice core and sediment core.
379

380 The CO₂ offset (or residual) is defined by:

$$381 \text{Offset}_{\text{CO}_2} = \text{CO}_2_{\delta^{11}\text{B-derived}} - \text{CO}_2_{\text{ice}} \quad (9)$$

382
383
384 The uncertainty on this offset (σ_{offset}) accounts for the uncertainty of the interpolated ice core CO₂
385 ($\sigma_{\text{CO}_2.\text{interpol}}$) and the one of the δ¹¹B-derived CO₂ ($\sigma_{\text{CO}_2.\delta^{11}\text{B-derived}}$), such as :

$$386 \sigma_{\text{offset}} = \sqrt{\sigma_{\text{CO}_2.\text{interpol}}^2 + \sigma_{\text{CO}_2.\delta^{11}\text{B-derived}}^2} \quad (10)$$

389 2.7 The relationship between δ¹¹B -derived pH and ΔF_{CO₂}.

390 The linear relationships between the relative CO₂ forcing ΔF_{CO₂} and pH are determined with a York
391 regression (York et al., 2004) that accounts for the uncertainty in both the independent and dependent
392 variable (i.e. x and y axes). The ice core CO₂ interpolation used to calculate ΔF_{CO₂} and uncertainty is
393 determined as described in section 2.6.3 (Hain et al., 2018).

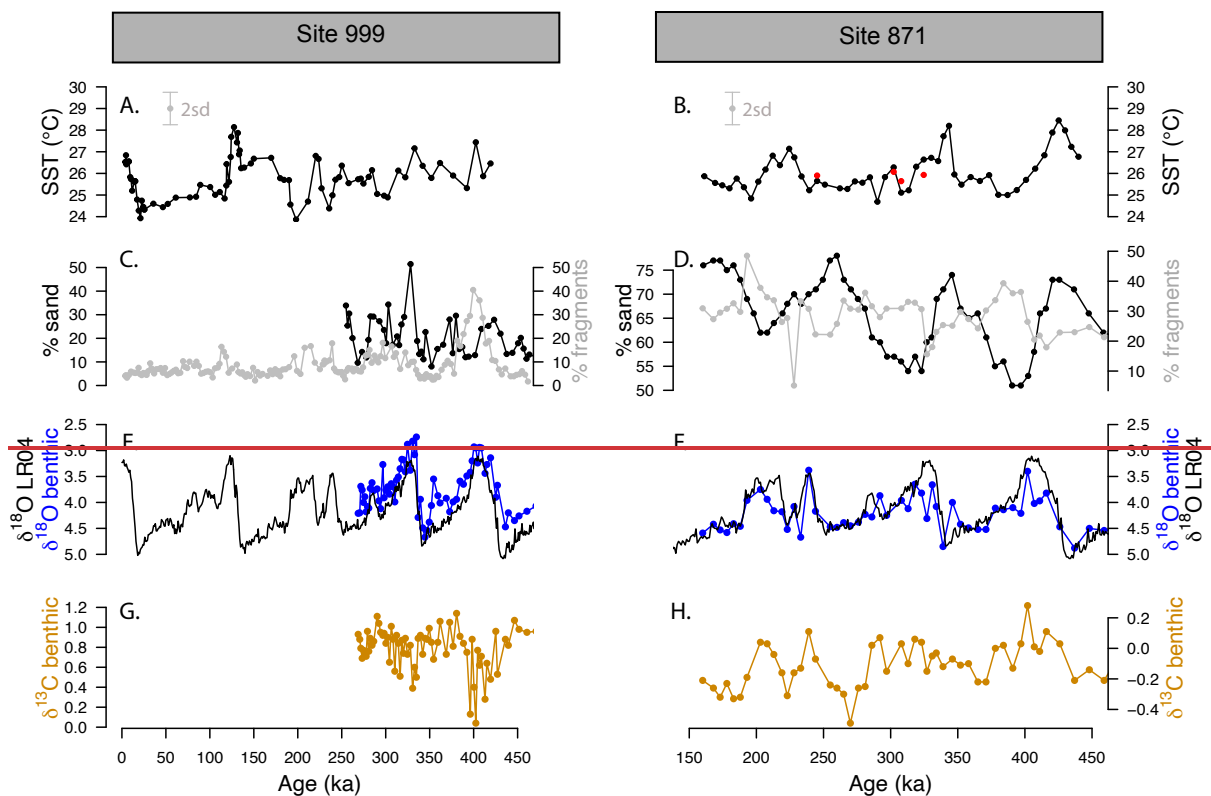
394 2.8 Optimising the *G. ruber* δ¹¹B borate-foraminifera calibration.

395 An optimised *G. ruber* calibration was obtained by minimising the root mean square error (RMSE) of
396 the average offset between δ¹¹B-derived CO₂ and ice core CO₂. The steps are illustrated in Figure S24.
397 In order to optimise the calibration, 10,000 simulations of δ¹¹B_{borate} and δ¹¹B_{foraminifera} from the calibration
398 of Henehan et al. (2013) were performed within their normally distributed uncertainty (1σ), from which
399 we defined the same number of linear models each including their slope and intercept. Then, we
400 calculate the equilibrium pH and resultant equilibrium δ¹¹B_{borate} from ice core CO₂ and the assumed
401 constant TA at each core site. The δ¹¹B_{borate} from the 10,000 linear models is then calculated and the
402 difference to the ice core-derived δ¹¹B_{borate} is determined. The linear model calibration that yields the
403 minimum RMSE between these two borate variables defines the new δ¹¹B_{borate-foram} calibration. To assess
404 the effect of δ¹¹B records from different sites we performed this exercise using the combined records
405 (from both sites 999 and 871), 999 only and 871 only (Figure S3) and show that using a record from
406 one particular site or the combination of sites yields similar CO₂ offsets (Table S3) and so here we use
407 the results from the combined sites. Unless indicated otherwise, to preserve a degree of independence,
408 the pH results presented in this study are calculated with the published calibration (Henehan et al.,
409 2013), and the results with the optimised calibration presented in section 4.2.6.

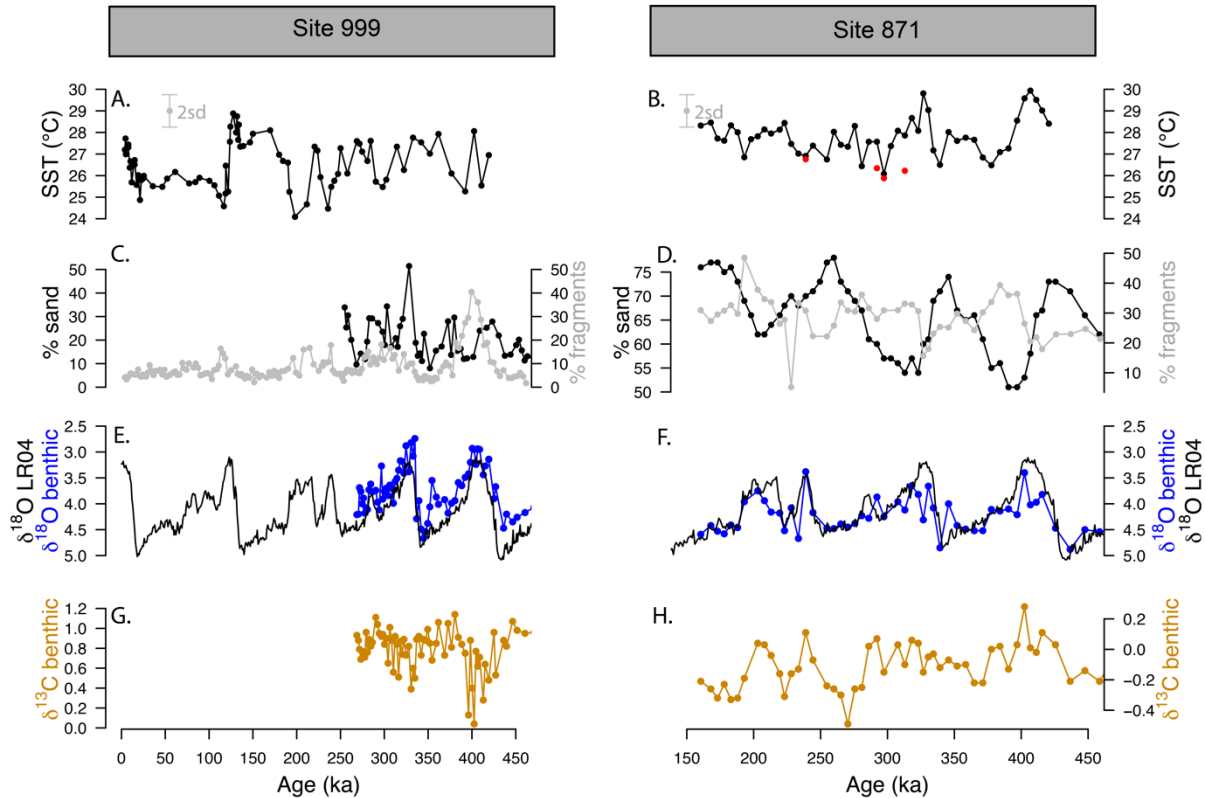
410 **3 Results.**

411 **3.1 Temperature and fragment counts.**

412 The SST at ODP Sites 999 and 871 show a cyclicity that agrees with the well-known glacial interglacial
 413 cycles of the late Pleistocene (Figure 2). ~~The Mg/Ca SST corrected for pH (Figure S2) shows lower~~
 414 ~~temperatures of about 0.2 to 2.5°C, yet the glacial variation structure is maintained.~~ The SST determined
 415 from *G. ruber sl* ~~Mg/Ca uncorrected~~ (red filled circles, Figure 2B) at Site 871, show ~~systematically~~
 416 ~~colder~~ equal or cooler temperatures (by 1-2 °C) than *G. ruber ss* (black filled circles). The
 417 fragmentation index (Figure 2D) at ODP 871 range from 20 to 50 % and follow the well-documented
 418 “Pacific style” dissolution cycles (Sexton and Barker, 2012) with well-preserved carbonate (low
 419 fragments) during glacials and less well-preserved carbonates (higher fragments) during interglacials.
 420 The percentage sand typically anticorrelates with fragmentation counts at both sites, although it is less
 421 clear at ODP 999, perhaps due to the shorter record available. Fragmentation counts reach maxima at
 422 ODP 999 of 20 % during interglacials and up to 50 % during marine isotope stage MIS 11 which is
 423 concomitant with the mid-Brunhes dissolution interval (MBDI, Barker et al., 2006). The fragmentation
 424 counts at ODP 871 show no substantive anomaly during the MBDI.



425
 426
 427
 428
 429

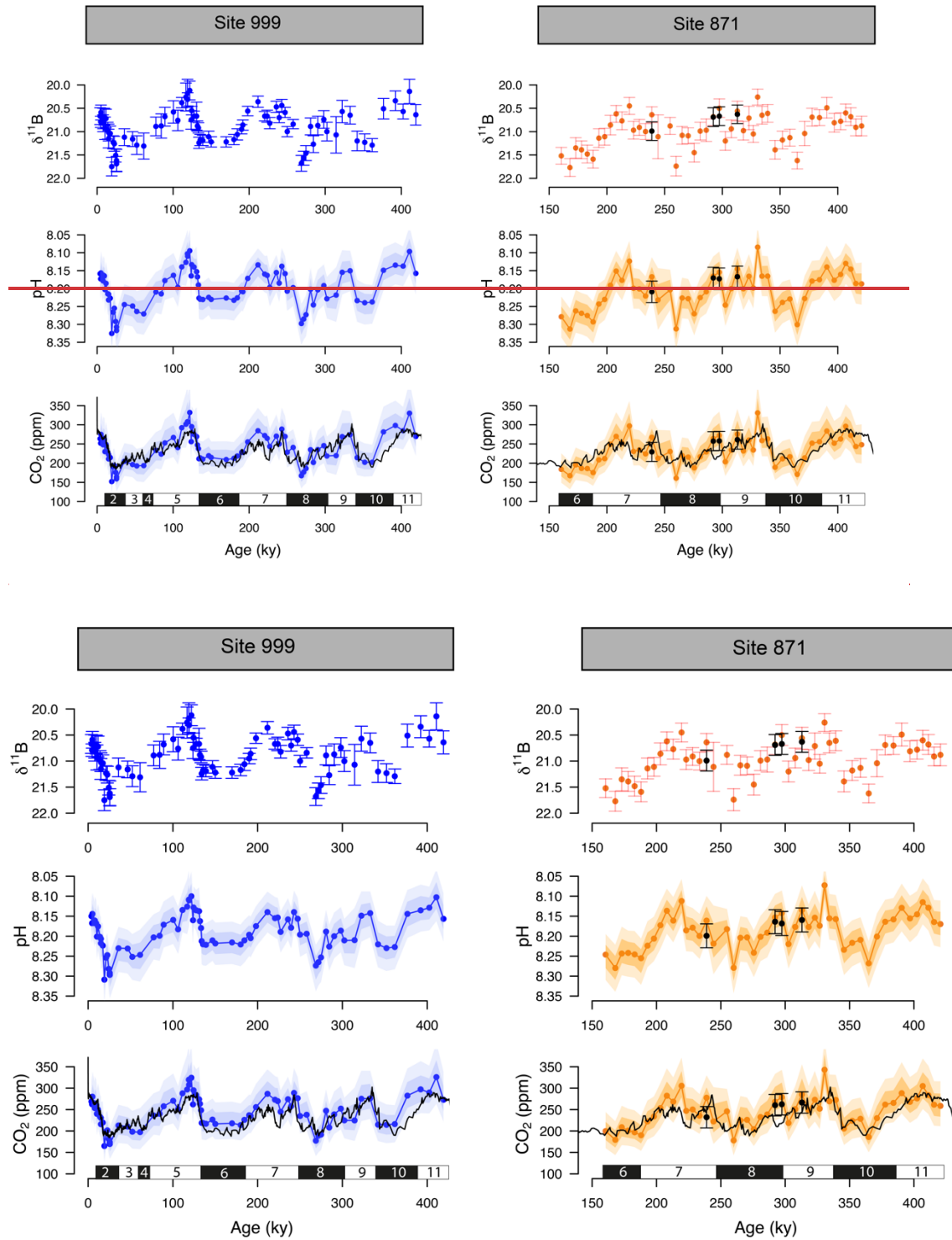


430
 431
 432 Figure 2. Mg/Ca derived temperature, coarse fraction (sand), fragmentation and benthic $\delta^{18}\text{O}$ and $\delta^{13}\text{C}$ at ODP
 433 sites 999 and 871. **A, B:** Temperature at ODP 999 (from *G. ruber ss*, black, Schmidt et al., 2006 [and this study](#))
 434 and ODP 871 (*G. ruber ss*, black, *G. ruber sl*, red, 2sd indicated by the grey error bar). **C, D:** Fragmentation index
 435 (light grey, data from Schmidt et al. (2006) for ODP 999) and sand (black line). **E, F:** Benthic *C. wuellerstorfi* ([Site](#)
 436 [999](#)) and *U. peregrina* ([Site 871](#)) $\delta^{18}\text{O}$ (blue) and LR04 benthic $\delta^{18}\text{O}$ stack (black). A correction of +0.478‰ is
 437 applied to our $\delta^{18}\text{O}$ of *C. wuellerstorfi* data in order to adjust for species offset [between *C. wuellerstorfi* and LR04](#).
 438 **G, H:** Benthic *C. wuellerstorfi* ([Site 999](#)) and *U. peregrina* ([Site 871](#)) $\delta^{13}\text{C}$ (orange).

439 3.2 pH and CO₂ reconstructions.

440 The $\delta^{11}\text{B}$, pH and $\delta^{11}\text{B}$ -derived absolute CO₂ (Figure 3) from Sites 871 and 999, show clear cyclicity
 441 related to glacial-interglacial cycles. The CO₂ values carry an average uncertainty of ± 48 ppm and the
 442 mean offset from the ice core CO₂ for a combination of the two records is $13 \pm 46 - 4.6 \pm 49$ (2σ) ppm
 443 showing that there is a minor overestimation of CO₂ using the boron method yet it agrees on average
 444 well within uncertainty. The RMSE of the CO₂ offset for the combined record is 265 ppm.

446 Despite the overall close agreement between $\delta^{11}\text{B}$ -derived CO₂ and ice core-derived CO₂, each of our
 447 $\delta^{11}\text{B}$ -CO₂ records exhibit some short-lived intervals where the offsets from the ice core record are larger.
 448 This is further revealed by the residual CO₂ and the identification of the data above the upper quartile
 449 (i.e. the upper 25% of the data, Figure S4.3). Those data do not appear to be randomly distributed and
 450 instead occur at ~ 100 ky, ~ 220 - 290 ky and ~ 390 ky at ODP Site 999, in all three cases during the early
 451 stages of the glaciation (except for the MIS 8 glacial at 280ky, Figure S4.3). The mismatches with the
 452 ice core at ODP Site 871 show a similar temporal pattern occurring at ~ 220 and ~ 300 and ~ 350 - 390
 453 ky (i.e. at glacial inceptions).
 454



455
456

457

458

459

460

461

462

463

464

465

466

Figure 3. $\delta^{11}\text{B}$, pH and boron-derived CO_2 at site 999 and 871. $\delta^{11}\text{B}$ of *G. ruber ss* and *sl* (top row), boron-derived pH (middle row) and CO_2 (bottom row) reconstruction from two core locations: ODP 999 (blue, this study and published data, Foster, 2008; Henchan et al., 2013; Chalk et al., 2017) and ODP 871 (orange, this study). The black line in the CO_2 panels is the composite Antarctic ice core CO_2 record (Bereiter et al., 2015). All $\delta^{11}\text{B}$ -derived data points are from *G. ruber ss* except black dots at ODP Site 871 measured on *G. ruber sl*. Numbers at the bottom of the CO_2 records represent marine isotope stages (Black boxes for glacial and white boxes for interglacial). Note the age scale is different between sites 999 and 871.

467

468 3.3 Contrasting $\delta^{11}\text{B}$ between morphotypes.

469 Within error, the few measurements of $\delta^{11}\text{B}$ *G. ruber sl* at ODP 871 all agree with $\delta^{11}\text{B}$ *G. ruber ss*
470 (Figure 3) albeit the $\delta^{11}\text{B}$ of *G. ruber sl* ~~are is~~ higher than *G. ruber ss* for all 4 data pairs available. The
471 CO_2 derived from *G. ruber sl* (Figure 3) is on average ~~22~~ ~~15~~ ppm lower than the one derived from *G.*
472 *ruber ss*; though the much lower resolution ($n=4$) impedes a thorough comparison at this stage. The
473 $\delta^{18}\text{O}$ and $\delta^{13}\text{C}$ of both morphotypes were compared for the whole records at ODP 871 (Figure S5.4) and
474 a cross-plot shows a moderate to good agreement between *G. ruber ss* and *sl* ($r^2=0.55$ and 0.22 for $\delta^{18}\text{O}$
475 and $\delta^{13}\text{C}$ respectively, Figure S6.5). This is in contrast to other studies (e.g. Wang et al., 2000; Steinke
476 et al., 2005) that show $\delta^{18}\text{O}$ in *G. ruber sl* to be systematically higher.

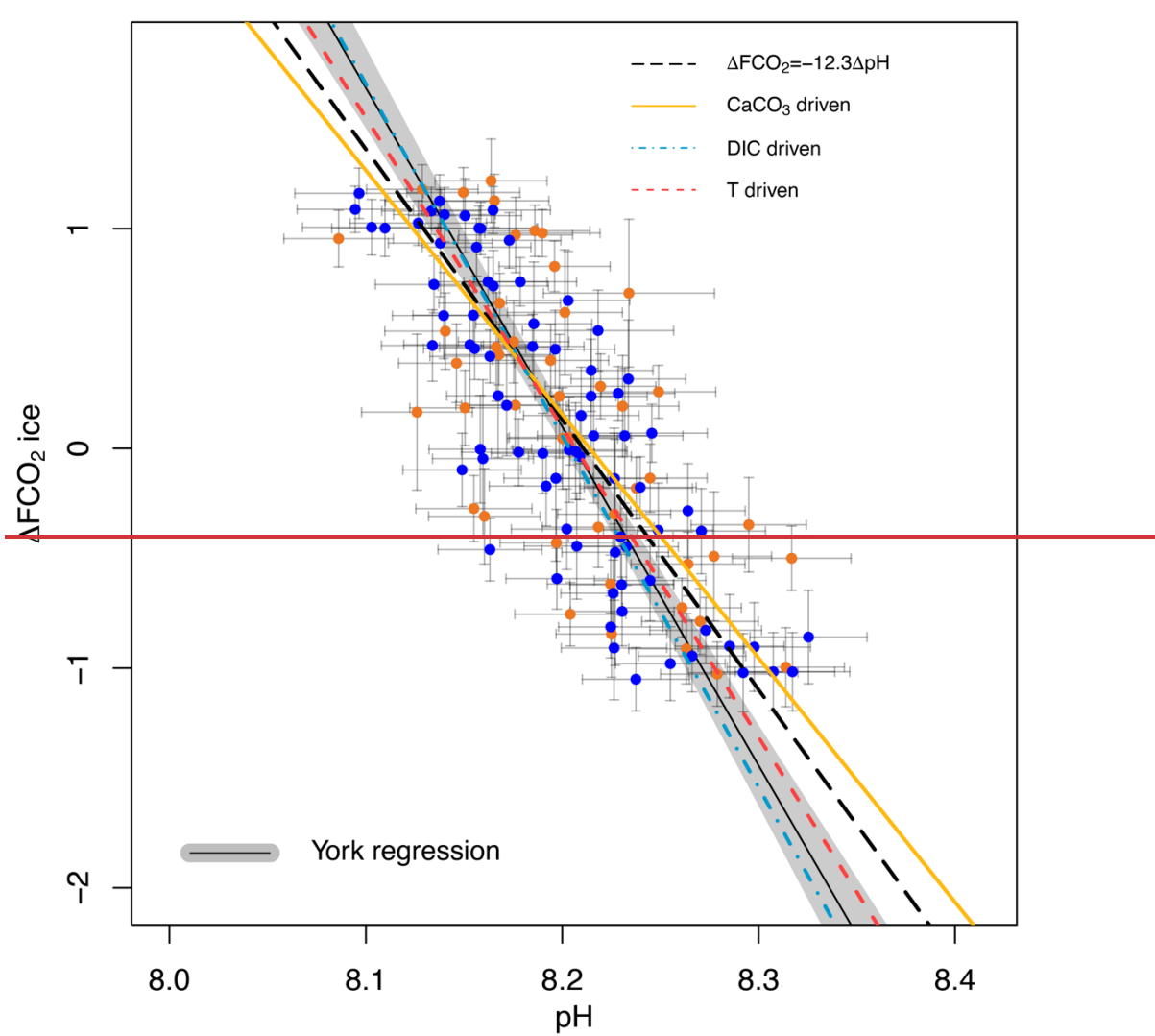
477 3.4 Dissolution experiments.

478 ~~The leaching experiments on *T. sacculifer* and *G. ruber ss* show a different response for the two species~~
479 ~~(Figure S6). While *G. ruber ss* show no significant variation in measured $\delta^{11}\text{B}$ under different~~
480 ~~treatments, *T. sacculifer* shows no systematic variations in $\delta^{11}\text{B}$ for the control and first two treatments~~
481 ~~(leached in 2 and 4 hours in 0.0001M HNO_3 , pH 4) but shows a $\sim 1\%$ shift (relative to the control)~~
482 ~~towards lighter $\delta^{11}\text{B}$ after 6 hours at pH 4.~~

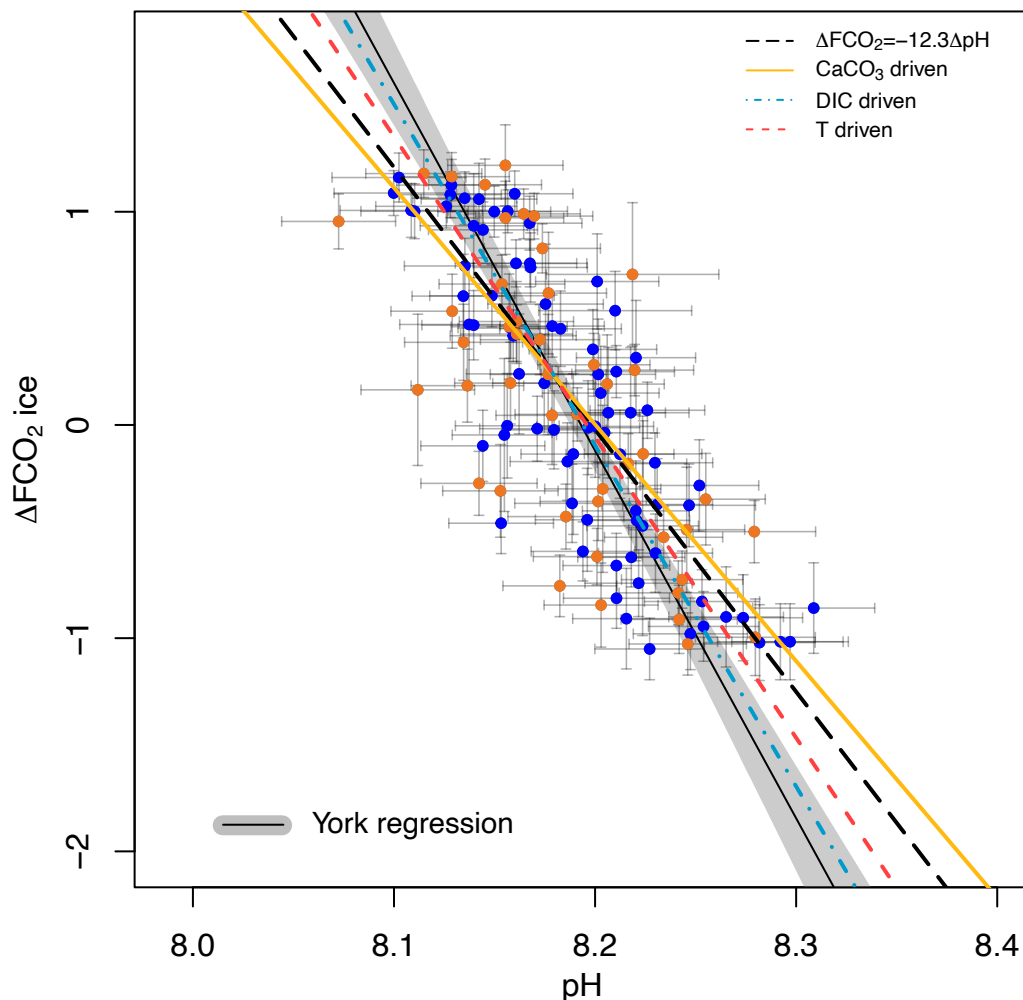
483 3.5.3.4 Relationship between $\delta^{11}\text{B}$ -pH and CO_2 forcing from the ice core.

484 A cross plot of $\delta^{11}\text{B}$ -derived pH CO_2 forcing from the ice core record for each of our marine core study
485 sites is shown in Figure 4 and is compared to the theoretically-derived approximate $\Delta\text{FCO}_2/\Delta\text{pH}$
486 relationships as adopted by Hain et al. (2018): $-1:1 \text{ W/m}^2$ (dashed black line); CaCO_3 addition/removal
487 ($-0.9:1 \text{ W/m}^2$ plain yellow line); DIC addition/removal ($-1.3:1 \text{ W/m}^2$ dotted-dashed blue); and
488 warming/cooling temperature forcing ($-1.1:1 \text{ W/m}^2$ dashed red). Our analysis includes full propagation
489 of uncertainty in pH, in contrast to Hain et al. (2018) who considered only the reported uncertainty of
490 $\delta^{11}\text{B}_{\text{borate}}$ in their validation exercise. In both cases the uncertainty in ΔFCO_2 accounts for the error in
491 interpolation arising when comparing age-uncertain $\delta^{11}\text{B}$ -derived pH with ΔFCO_2 from the well-dated
492 and high-resolution ice core CO_2 record (see methods 2.7 and 2.6 for details). This treatment of ΔFCO_2
493 uncertainty is dominated by the spread of ice core CO_2 data points within the $\delta^{11}\text{B}$ age uncertainty. The
494 data are fitted with a York-type regression (thin black line; York et al., 2004) where the grey envelope
495 represents the uncertainty of the linear relationship that best represents the data (i.e., the envelope is not
496 the prediction interval), considering the uncertainty in pH and ΔFCO_2 . The regressed slope is $\Delta\text{F}/\Delta\text{pH} =$
497 -17.2 ~~15.42~~ $\pm 10.8 \text{ W/m}^2$ ($-1.42:1$ relative to basic formalism) and shows a good agreement with the
498 theoretical temperature and DIC driven relationships.

499 The effect of the uncertainty assigned to pH (fully propagated or using the measurement uncertainty of
500 the boron isotope) on the regressed slope is shown in Figure S7. The slope of the York regression when
501 using the uncertainty from $\delta^{11}\text{B}$ only, as in Hain et al. (2018), shows a ~~very~~ close agreement with the
502 basic formalism, with a slope of $\Delta\text{F}/\Delta\text{pH} = -13.7$ ~~12.4~~ $\pm 0.3 \text{ W/m}^2$, ($-1.1:1$ relative to the basic
503 formalism) but with a unsatisfactory goodness of fit (mean square ~~d~~ weighted deviation, mswd) of ~~5.36~~,
504 whereas propagating the full pH uncertainty based on our iterative Monte-Carlo simulations improves
505 goodness of fit to ~ 0.94 at a $\Delta\log_{10}\text{CO}_2/\Delta\text{pH}$ of $-1.42:1$ (Figure 4).



506



507
508
509

Figure 4. Ice core based ΔFCO_2 (CO_2 forcing) vs. $\delta^{11}\text{B}$ -based pH for ODP 999 (blue filled circles, this study and published data from Foster, 2008; Henchan et al., 2013; Chalk et al., 2017) and 871 (orange filled circles). The lines show the relationship between ΔFCO_2 and pH for the simplified formalism (see method) $\Delta\text{FCO}_2 = -12.3\Delta\text{pH}$ (black dashed line), and when driven by changes in DIC only (blue, $\Delta F/\Delta\text{pH} = -16 \text{ W/m}^2$), CaCO_3 (yellow, $\Delta F/\Delta\text{pH} = -11.1 \text{ W/m}^2$) and temperature T (red, $\Delta F/\Delta\text{pH} = -14.1 \text{ W/m}^2$). The York regressed line (black line and grey shade) falls close to the DIC-driven line (blue), between the theoretical only pH driven line (black) and CaCO_3 -line (yellow).

517 **4 Discussion.**

518 **4.1 Cyclicity in foraminifera preservation.**

519 Percentage fragments and sand fraction ($> 63\mu\text{m}$) at both studied core sites are anticorrelated and show
520 a clear cyclicity, with better preservation of carbonates during glacial periods (Figure 2). The
521 anticorrelation is clearer at ODP Site 871 where we have the longest record (Figure 2). Preservation in
522 the Pacific (Farrell and Prell, 1989) show improved (poorer) preservation during glacial (interglacial)
523 and this pattern seems to have originated after the mid Pleistocene transition (MPT) (Sexton and Barker,
524 2012). The origin of these cycles could be a combination of enhanced ventilation during glacials in the

525 Pacific (Sexton and Barker, 2012), or increased burial due to enhanced global alkalinity following a
526 decrease in burial in the Atlantic (Cartapanis et al., 2018). However glacial periods seem to have been
527 accompanied by a diminution in oxygenation in the deep Pacific (Anderson et al., 2019) that may have
528 also impacted preservation.

529
530 ~~Sexton and Barker (2012) suggest that this Pacific Ocean pattern of preservation (Farrell and Prell,~~
531 ~~1989) initiated after the mid Pleistocene transition (MPT) around 1 Ma, and that preservation cycles in~~
532 ~~the Pacific prior to MPT showed a more “Atlantic style” of dissolution with better (poorer) preservation~~
533 ~~occurring during interglacials (glacials).~~

534 ~~Several data sets (deep oxygen and carbon isotopes, carbonate ion data, and sortable silt) point towards~~
535 ~~a strengthening of ventilated deep Pacific waters (lower circumpolar deep water LCDW) that lead to~~
536 ~~the better preservation during glacials in the Pacific after the MPT (Sexton and Barker, 2012).~~

537
538 The observation that the fragmentation records of sites 999 and 871 covary is likely attributable to the
539 different water masses that fill the Caribbean basin relative to the rest of the Atlantic basin. During
540 glacials, the deep Atlantic is filled by nutrient- and carbon-rich corrosive southern sourced waters
541 (Antarctic Bottom Water, ~~AABW~~) with a reduced contribution from the less corrosive, nutrient-poor
542 North Atlantic Deep Water (~~NADW~~) (Oppo and Lehman, 1993) causing calcareous sediments in the
543 deep Atlantic Ocean >2500 m to be less well-preserved during glacials than interglacials. The opposite
544 pattern of dissolution is seen in the Caribbean because shoaling of the northern sourced waters during
545 glacials produces a mid-depth well-ventilated water mass that feeds into the Caribbean through its
546 deepest sill (~1900 m, Johns et al., 2002). Thus the deep Caribbean is filled with less corrosive waters
547 during glacials than interglacials improving the preservation of carbonate during glacials in a similar
548 pattern to a Pacific styled dissolution cycle albeit in response to Atlantic circulation changes. During
549 interglacials, the Northern sourced waters are mixed with corrosive southern sourced waters (Antarctic
550 Intermediate Waters and upper circumpolar deep waters) leading to less well-preserved sediments.

551 4.2 Causes of offset between $\delta^{11}\text{B}$ –derived and ice core CO_2 .

552 The $\delta^{11}\text{B}$ -derived CO_2 record from both of our study sites is in very good agreement with the ice core
553 record, with an average offset for combined both cores of 13±46 (2 σ) ppm ~~4.6 ±49 (2 σ) ppm~~ and
554 corresponding RMSE of 24.7-26 ppm. ~~The CO_2 -offset calculated with Mg/Ca SST corrected for pH is~~
555 ~~shown in Figure S8 for comparison and the average is -4.8 ±42 (2 σ) ppm, showing a reduced offset of~~
556 ~~9 ppm compared to treatment with no pH correction on SST (a difference of 11 ±14 (2 σ) and 8 ±12~~
557 ~~(2 σ) ppm at ODP site 871 and 999, respectively). This difference is due to the pH correction lowering~~
558 ~~the SST estimates on average without greatly changing the temporal structure of pH and CO_2 -offsets.~~

559 ~~In both treatments, the RMSE is smaller than the average CO_2 uncertainty of ±48 ppm (2 σ , 95%~~
560 ~~confidence) for each datapoint.~~ However, the minor CO_2 offsets observed in both records do not appear
561 to be random and tend to fall during the first half of each glacial cycle (Figure S4 S2). In order to have
562 the highest confidence in CO_2 reconstructions using $\delta^{11}\text{B}$, this pattern warrants further investigation
563 (see below). ~~We only discuss the CO_2 records calculated without a pH correction on SST.~~

566 4.2.1 Comparison between morphotypes of *G. ruber*

567 If as others suggested (e.g. Wang et al., 2000; Steinke et al., 2005; Numberger et al., 2009) *G. ruber sl*
568 and *G. ruber ss* occupied different depth habitats, then inadvertent sampling of the cryptic *G. ruber sl*
569 morphotype might conceivably produce the biases we observe between $\delta^{11}\text{B}$ -derived CO_2 and
570 atmospheric CO_2 from the ice cores. However, while our Mg/Ca-derived temperatures for *G. ruber sl*
571 and *G. ruber ss* display variable offsets, they are within uncertainty (Figure 2) and our $\delta^{18}\text{O}$ and $\delta^{13}\text{C}$
572 data for the two morphotypes at ODP 871 show a good agreement with no consistent differences (Figure
573 S5S4). Thus, while the water column profile of $\delta^{18}\text{O}$ and $\delta^{13}\text{C}$ can be affected by factors other than

574 temperature, salinity and biological productivity (e.g, carbonate ion effect, Spero et al., 1997), overall,
575 our data suggest that the two morphotypes we analysed shared similar depth habitat preferences.

576 Henahan et al. (2013) found that *G. ruber ss* and *sl* record similar $\delta^{11}\text{B}$ in core-top sediments, and
577 through necessity, used mixed morphotypes in their culture study. The $\delta^{11}\text{B}$ -derived pH and CO_2 for *G.*
578 *ruber sl* examined here are consistently higher and lower, than *G. ruber ss* by around +0.02 0.05-pH
579 units and -22 +5-ppm CO_2 , on average, respectively (Figure 3). This is contrary to expectation if *G.*
580 *ruber sl* lived in deeper more acidic waters as suggested by other studies (Wang et al., 2000; Steinke et
581 al., 2005), but consistent with some data sets that show that the habitat of *G. ruber ss* and *sl* can vary
582 by location and seems to be dependent on local productivity (Numberger et al., 2009). Other data sets
583 from the Atlantic and Indian ocean nevertheless show similar Mg/Ca between both morphotypes (Gray
584 et al., 2018). We acknowledge that the scarcity of *G. ruber sl* in our samples means that our data set for
585 this morphotype is too small to draw firm conclusions and this warrants further investigation at other
586 study sites. Nonetheless, the closeness of the morphotypes in terms of $\delta^{11}\text{B}$ and depth habitat throughout
587 our record implies any inadvertent sampling of *G. ruber sl* in the *G. ruber ss* fraction in this study and
588 location would not significantly bias our reconstructions.

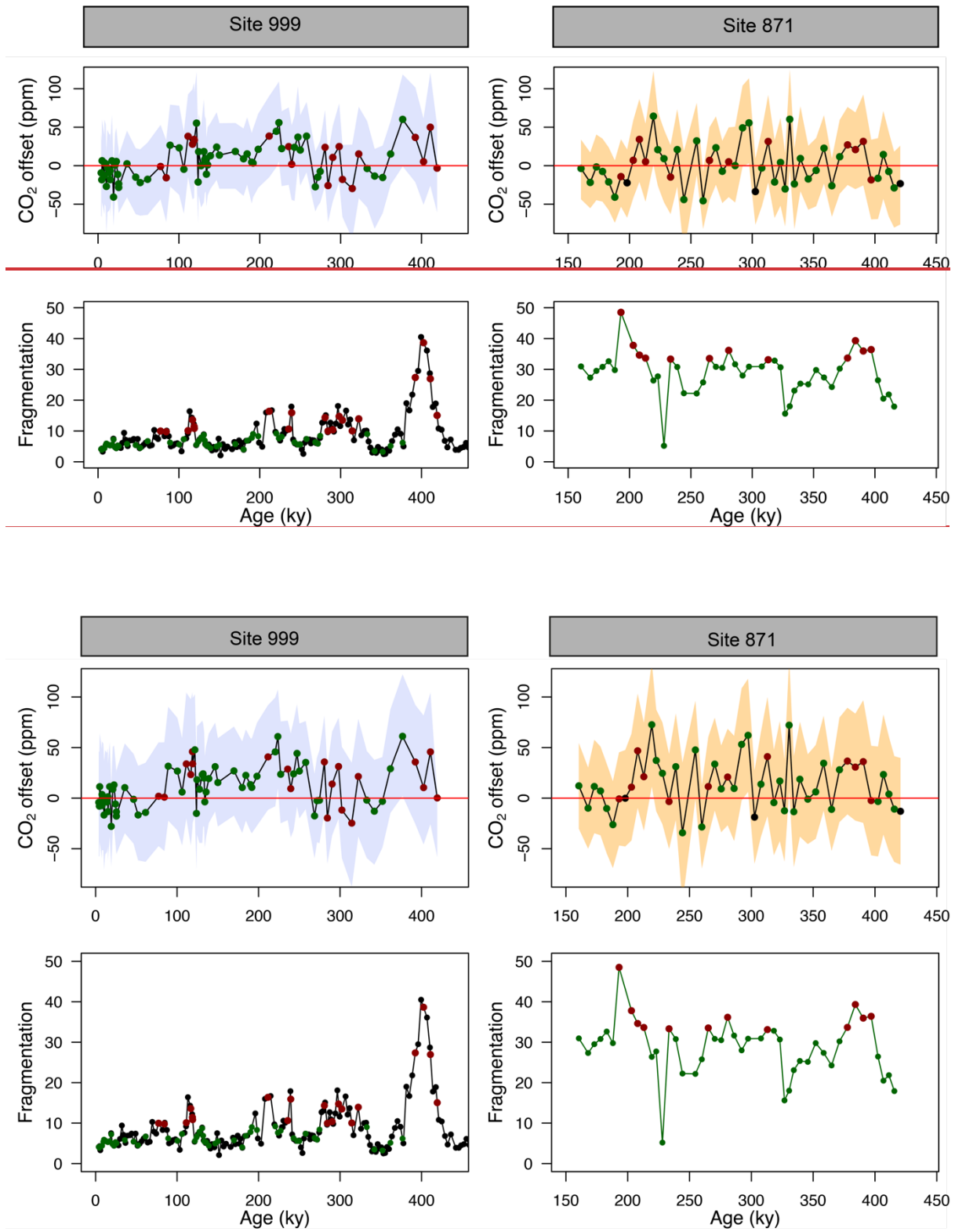
589 4.2.2 Change in upwelling and CO_2 disequilibrium.

590 ODP sites 871 and 999 are both located today in stratified oligotrophic environments with a deep
591 modern thermocline (base of the thermocline is at ~ 200 and 400 m at ODP 871 and 999, respectively;
592 Olsen et al., 2016). It should be noted, however, that both sites are situated relatively close to regions
593 displaying $\Delta\text{pCO}_2 > 40$ ppm (Figure 1). However, if local upwelling occurred over the study interval,
594 or if these areas of upwelled water expanded, we would expect these periods to be characterised by
595 relatively low SST, high surface $\delta^{18}\text{O}$, and low surface $\delta^{13}\text{C}$ due to an increased influence of deep
596 colder and more remineralised waters. The identified anomalous intervals in residual CO_2 at ODP 871
597 (e.g at ~ 210 , ~ 290 ky, Figure 5) show no particular anomaly in planktonic C and O isotopes (Figure
598 S5 S4) or in SST (Figure 2, Figure S8 S9), ruling out significant variations in upwelling at that site.
599 The Mg/Ca-derived SST record of nearby Site MD97-2140 (Figure S8) from the Western Pacific
600 warm pool (de Garidel-Thoron et al., 2005) a location outside of the upwelling from the Pacific cold
601 tongue, confirms this view in that the periods of high CO_2 offset at Site 871 are not associated with
602 relatively cold periods at site MD97-2140. Equally, no SST anomaly was identified at ODP 999 to be
603 coincident with the intervals of high residual CO_2 (Figure S9). Foster and Sexton (2014) have also
604 reconstructed CO_2 zonally across the equatorial Atlantic and the Caribbean and showed that while
605 enhanced disequilibrium was detected in the eastern Atlantic, for the last 30 ky at least, Site 999 has
606 remained in equilibrium with the atmosphere. This suggests the CO_2 anomalies revealed in Figure 5
607 are not the result of enhanced local disequilibrium via sub-surface water mixing. Whilst SST is a first
608 order constraint on upwelling, we acknowledge future constrains are needed using paired proxies of
609 local CO_2 , temperature and productivity to evaluate changes in local CO_2 fluxes.

610

611 4.2.3 Partial dissolution.

612 The CO_2 derived from *G. ruber* $\delta^{11}\text{B}$ at ODP 999 and 871 appears to show, at first order at least, positive
613 CO_2 offset during periods of high fragmentation (~ 100 , ~ 210 , ~ 400 ky, red filled circles in Figure 5,
614 defined by the upper 25% quantile of fragments) following a “Pacific style” dissolution cycle (better
615 preservation and lower fragmentation during glacial periods). Periods of high fragmentation at ODP
616 Site 999 and 871 both (incidentally) correspond to a positive CO_2 offset 65 and 75% of the time
617 respectively, and 35 and 25% 25% of the time to a negative or no (i.e. ± 10 ppm) CO_2 offset, (note that
618 values ± 10 ppm close to 0 were omitted in the criteria for positive or negative offset this calculation).
619 We also note that almost all CO_2 offsets uncertainty (2σ) overlap with the 0 line, hence the percentage
620 of CO_2 offset that are above or below the 0 line should be interpreted with caution.



621
622
623
624

625
626
627
628
629
630
631
632
633
634

Figure 5. Top panels: CO₂ offset (defined as $\text{offset} = \text{CO}_2_{\delta 11\text{B-derived}} - \text{CO}_2_{\text{icc}}$) for ODP Sites 999 (this study and Chalk et al., 2017) and 871. See text for error bars calculations. Bottom panels: fragmentation index at Site 999 (Schmidt et al., 2006) and 871 (this study). Red dots in the lower panels are the fragments above the upper quartile (and corresponding CO₂ in the upper panel, red dots). Green dots represent periods of low fragments below the upper quartile (and corresponding CO₂ in the upper panel, green dots).

635 In detail however, a cross-plot of fragment counts and CO₂ offset (Supplementary Figure S9 S10) fitted
636 with a linear regression shows no significant correlation for both core site 999 ($r^2=0.060-07$, $p=0.03$
637 $0-02$) and 871 ($r^2=0.002 0-01$, $p=0.77 0-62$). Although it should be noted that this simple linear
638 regression presupposes a linear relationship between the variables and does not account for the
639 significant uncertainty in both CO₂ offset and fragmentation index. In particular, the CO₂ offset carries
640 the uncertainty from the interpolated ice core CO₂ (see methods). Fragment counts at ODP 999 also
641 come with the additional uncertainty related to the interpolation of the record of Schmidt et al. (2006),
642 whereas fragment counts and $\delta^{11}\text{B}$ -derived CO₂ at 871 are measured on the same samples. A cross-
643 correlation function also shows no correlation between CO₂ offset and fragmentation (Figure S10 S14).

644 While it seems unlikely the small offsets observed are fully explained by partial dissolution, the positive
645 CO₂ offsets observed during some periods of high fragmentation index (Figure 5), are in line with trends
646 observed in other species like *T. sacculifer* (sacc). For instance field studies observed lower $\delta^{11}\text{B}$ in *T.*
647 *sacculifer* for core-top samples from deeper ocean sites bathed by waters with low calcite saturation
648 state (Hönisch and Hemming, 2004, Seki et al., 2010). Tests of *T. sacculifer* can contain a significant
649 proportion of gametogenic calcite (ranging 30 to 75% of the weight of pregametogenic calcite, Bé,
650 1980; Caron et al 1990) which forms at the end of the life cycle in deeper lower pH cold waters. It has
651 been suggested that $\delta^{11}\text{B}$ is lower in gametogenic calcite than in the primary test (Ni et al., 2007)
652 reflecting the digestion and expulsion of symbionts (Bé et al., 1983) before gametogenesis, driving a
653 relative acidification of the micro-environment (no CO₂ uptake by photosynthesis) around the
654 foraminifera (Zeebe et al. 2003; Hönisch et al., 2003; Henehan et al. 2016), and movement to deeper
655 more acidic waters during that life-stage. It has been shown that this gametogenic calcite is more
656 resistant to dissolution (Hemleben et al., 1989; Wycech et al., 2018) resulting in partial dissolution
657 acting preferentially on ontogenic calcite, and driving $\delta^{11}\text{B}$ in the residual test to lower isotopic
658 composition.

659 However, while the decrease in $\delta^{11}\text{B}$ in tests of *T. sacculifer* found in corrosive waters is well explained
660 by the lighter isotopic composition of gametogenic calcite, *G. ruber* tests do not contain such
661 gametogenic calcite (Caron et al., 1990). Hence, if the observed occasional decrease in $\delta^{11}\text{B}$ (low pH,
662 high CO₂) was caused by partial dissolution, it needs to be explained by other processes. It should also
663 be considered that alternative measures and proxies of dissolution (e.g. benthic B/Ca as an indicator of
664 bottom water carbonate ion concentration) may yield more quantitative constraints on the importance
665 of dissolution in generating our observed CO₂ offsets. Some studies have shown that laboratory
666 dissolved specimens of *T. sacculifer* (Sadekov et al., 2010) and naturally dissolved specimens of *G.*
667 *ruber* (Iwasaki et al., 2019) undergo targeted partial preferential dissolution of the shell. However,
668 variations in intra-shell $\delta^{11}\text{B}$ are currently unknown due to limitations in laser ablation techniques that
669 currently impede a direct evaluation of $\delta^{11}\text{B}$ heterogeneity in foraminifera chambers. Future studies are
670 needed to constrain the $\delta^{11}\text{B}$ spatial distribution in foraminiferal shells caused by potential variations in
671 $\delta^{11}\text{B}$ from dissolution, ontogeny (e.g. Meilland et al., 2021) and/or vital effects (e.g. change in
672 photosymbiotic activity throughout the life cycle, Lombard et al., 2009, Henehan et al., 2013, Takagi
673 et al., 2019). In the absence of these constraints, we conclude that partial dissolution is unlikely to be a
674 significant driver of the $\delta^{11}\text{B}$ -CO₂ records we present here. Even though it was thought to be a species
675 susceptible to dissolution (Berger, 1970), we confirm that the $\delta^{11}\text{B}$ of *G. ruber* appears more resistant
676 to dissolution-driven modification than *T. sacculifer*.

677 678 4.2.4. Effect of dissolution on Mg/Ca and calculated CO₂.

679 The direction of change of Mg/Ca with partial dissolution is towards lower ratios in partially dissolved
680 foraminifera (e.g. Brown and Elderfield, 1996; Dekens et al., 2002; Fehrenbacher and Martin, 2014). If
681 the Mg/Ca is impacted during periods of high fragmentation, the lower ratio would result in lower
682 temperatures leading to lower calculated CO₂ values (equation 7). This effect is opposite to the
683 occasional positive deviation of CO₂ observed during intervals of high fragmentation at ODP Site 999.

684 While the weak correlation between fragmentation and CO₂ precludes a firm interpretation of
 685 dissolution effect, we conclude that the effect of partial dissolution on Mg/Ca ratio and resulting CO₂
 686 (if any) ~~is~~ are negligible and not responsible for the CO₂ offsets observed during intervals of high
 687 fragmentation.
 688

689 4.2.5. *Change in the second carbonate parameter, alkalinity.*

690 Past changes in TA are poorly constrained, although some constraints are starting to emerge for the late
 691 Quaternary (e.g. Cartapanis et al., 2018). However, since pH is directly determined by δ¹¹B, pH defines
 692 the ratio of alkalinity to DIC (see supplementary information [S11 S12](#)). Hence, at any given pH, any
 693 change in alkalinity must be counteracted by a change in DIC, which has the opposing effect on CO₂.
 694 This is demonstrated by the tight relation between pH and CO₂ highlighted by our data (Figure 4). The
 695 largest residual CO₂ is ~50 ppm at ODP 999. To produce an effective alkalinity-driven change in CO₂
 696 of this magnitude at a given pH requires an alkalinity reduction of about ~300 to 500 μmol/mol
 697 (supplementary Figure [S12 S13](#)). This is far larger than any expected change over a glacial cycle
 698 (Cartapanis et al., 2018, Hönisch et al., 2009). We therefore rule out varying TA as the cause of the
 699 minor CO₂ offsets observed (Figure 5).

700 4.2.6 *Improving the δ¹¹B -pH G. ruber calibration*

701 A further potential cause for the minor offsets observed between δ¹¹B-derived and ice core CO₂ could
 702 be a small inaccuracy in the calibration between δ¹¹B of foraminifera and borate for *G. ruber* (Henehan
 703 et al., 2013). Having the ice core data to compare with δ¹¹B-derived CO₂ offers an opportunity to explore
 704 the effect of altering the input variables of the pH-CO₂ calculation to see if doing so improves the fit to
 705 ice-core values. Note that such an exercise is for illustrative purposes only because we seek to retain
 706 the independence offered by the δ¹¹B-calibrated data in the context of CO₂ forcing (section 4.3).
 707 Nonetheless, in future work we suggest this calibration can be applied in tandem to the empirical
 708 relationship of Henehan et al. (2013). The published (Henehan et al., 2013) and obtained optimised
 709 calibration (Figure [S13 S14](#)) are:

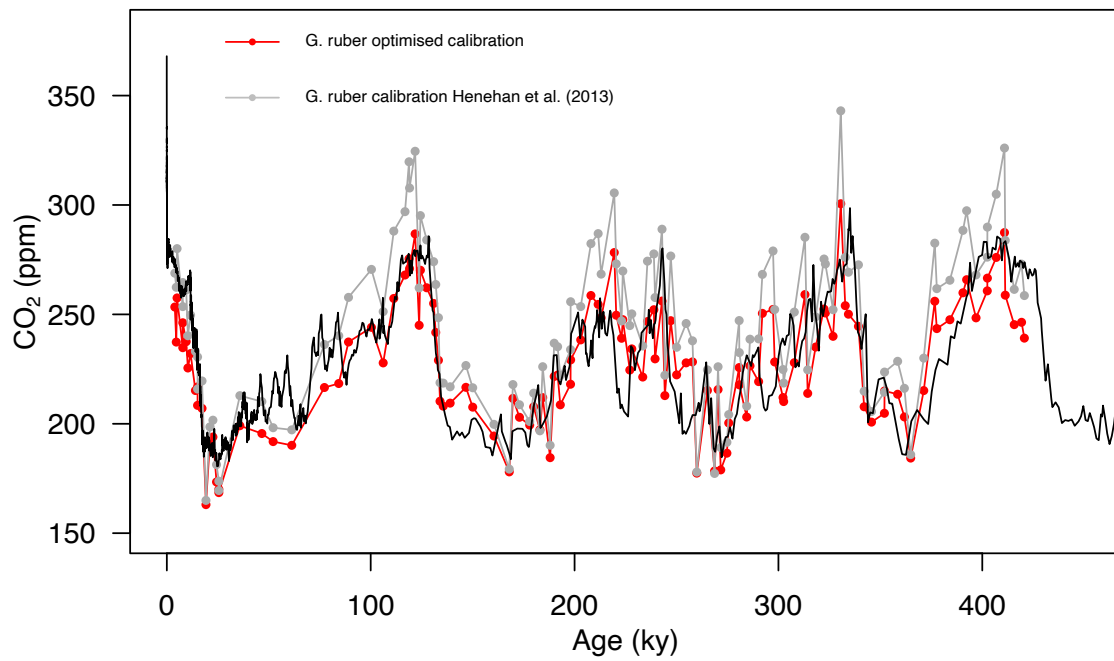
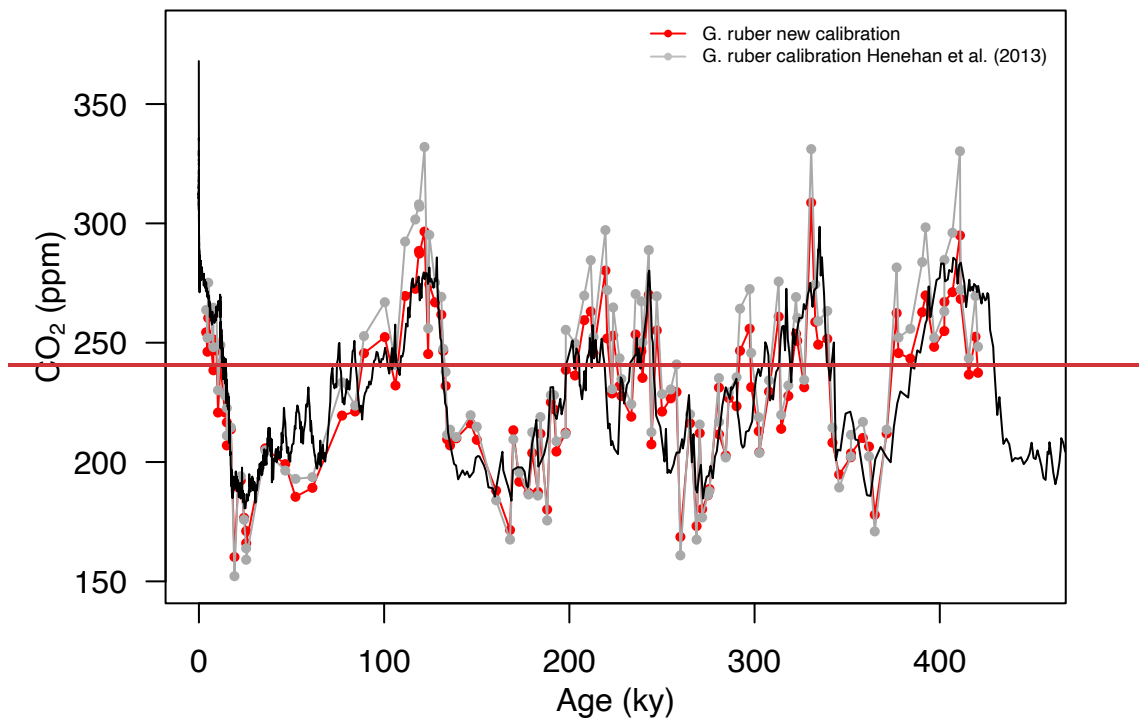
710
$$\delta^{11}\text{B}_{\text{borate}} = \frac{\delta^{11}\text{B}_{\text{foram}} - 8.87(\pm 1.52)}{0.60(\pm 0.09)} \quad (\text{Henehan et al., 2013})$$

711 ~~$$\delta^{11}\text{B}_{\text{borate}} = \frac{\delta^{11}\text{B}_{\text{foram}} - 6.46}{0.72} \quad (\text{optimised calibration})$$~~

712
$$\delta^{11}\text{B}_{\text{borate}} = \frac{\delta^{11}\text{B}_{\text{foram}} - 6.49}{0.71} \quad (\text{optimised calibration})$$

713

714 The newly calculated CO₂ with the updated calibration shows an improved average CO₂ offset (Figure
 715 6) of ~~-4 ± 36 (2σ)~~ -3.43 ± 41 (2σ) ppm (vs 13 ± 46 (2σ) ppm ~~4.6 ± 49 (2σ) ppm~~ with the calibration of
 716 Henehan et al., 2013) and an RMSE of 18 ppm ~~20.68 ppm~~ (vs. 26 ~~25~~ ppm with the published
 717 calibration).
 718
 719



725 Figure 6. –Composite $\delta^{11}\text{B}$ -derived CO_2 from both core sites 999 and 871 using the published $\delta^{11}\text{B}_{\text{borate-foram}}$
726 calibration (grey points, Henehan et al., 2013) and the ~~optimised improved~~ calibration (red points). The black line
727 is the Antarctic composite ice core CO_2 record (Bereiter et al., 2015).

728 When analysing the CO_2 offset using the optimised *G. ruber* calibration and the fragmentation index
729 at each core location (same approach as Figure 5), we observe that intervals of high fragments
730 (defined as values above the upper quartile) are no longer preferentially associated with positive CO_2
731 offset (Figure S14 15). ~~Intervals of high fragments at site 999 have 50% chance of corresponding CO_2~~
732 ~~with positive offsets to the ice core (and 50% with negative offset to the ice core). Intervals of high~~
733 ~~fragments at site 871 have 56% of corresponding CO_2 with a positive offset to the ice core (and 44%~~
734 ~~with a negative offset to the ice core). Intervals of high fragments occur 5% and 33% of the time, at~~
735 ~~Sites 999 and 871, respectively, during positive CO_2 offsets (and 95 and 67% of the time during~~
736 ~~negative or no offset to the ice cores).~~

737 This analysis shows that a small change in the borate *G. ruber* $\delta^{11}\text{B}$ calibration is enough to improve
738 the fit to the ice core and diminishes the apparent correlation between high fragmentation and
739 CO_2 offset ~~does not cause any visual correlation between CO_2 offset and fragmentation index~~ (Figure
740 S14 S15), and that uncertainty in the $\delta^{11}\text{B}_{\text{foram-borate}}$ calibration of Henehan et al. (2013) can – at least
741 partly – explain the minor discrepancies we observe between $\delta^{11}\text{B}$ -derived and ice core CO_2 .

742 4.3 Relative CO_2 forcing and pH.

743 Our new pH data, added to the existing compilation, show a good agreement with the formalism
744 defined by Hain et al. (2018; Figure 4). It should be noted that CO_2 in this case is provided by the ice
745 core directly and is not estimated from the $\delta^{11}\text{B}$ -derived pH. As discussed above, because these two
746 proxies are independent of one another, the slope of their relationship may be used to interrogate the
747 mechanisms of CO_2 change. Our data fall between the CaCO_3 (yellow plain line) and the DIC (dotted-
748 dashed blue line) end-members suggesting that the CO_2 change observed on glacial-interglacial
749 timescales was driven by a mix of mechanisms rather than to a single cause. This is in line with
750 studies that require a number of mechanisms to explain glacial interglacials CO_2 change such as the
751 ~~(soft tissue pump, carbonate compensation pump, and solubility thermal pump, (e.g. Brovkin et al.,~~
752 ~~2007, Kohfeld and Ridgwell, 2009, Hain et al., 2010, Chalk et al., 2019, Sigman et al., 2021), and the~~
753 ~~disequilibrium pump (Eggleston and Galbraith, 2018)~~. We note that this is a preliminary
754 interpretation because of the sensitivity of our finding to pH uncertainty (section 3.45, Figure S7). To
755 overcome this ambiguity in estimating past ΔFCO_2 and to better deconvolve the driving mechanisms
756 of glacial/interglacial CO_2 change, we recommend that future studies collect pH data at higher
757 temporal resolution to examine the change in slope through a glacial cycle and strive to further
758 quantify and reduce uncertainties related to pH determination.

759 The close agreement of the pH and ice core CO_2 data with the theoretical relationships has a number of
760 consequences for the reconstruction of CO_2 change during periods of Earth history beyond the ice core
761 CO_2 and climate records where constraints on $\delta^{11}\text{B}_{\text{sw}}$ and the second carbonate parameter and
762 temperature are uncertain. The ΔpH formalism still requires an estimation of $\delta^{11}\text{B}_{\text{sw}}$ and temperature
763 (for the pK_B term, equation 5) however, as discussed in Hain et al. (2018), while absolute reconstruction
764 of pH is significantly influenced by estimates of $\delta^{11}\text{B}_{\text{sw}}$ and temperature, reconstruction of relative pH
765 change (ΔpH) is inherently much less sensitive to these input variables.

766 Reconstructing ΔFCO_2 from ΔpH is ideally applicable only on relatively short timescales less than 1
767 Myrs, when $\delta^{11}\text{B}_{\text{sw}}$ is likely to be invariant constant given the multi-million year residence time of
768 boron in the ocean (Lemarchand et al., 2000, Greenop et al., 2017). Furthermore, to reconstruct ΔFCO_2
769 (and thus climate sensitivity to CO_2), the formalism can be applied as long as, in equation 2, ΔpH
770 remains the overwhelming control. This is dependent on the residence time of carbon in the ocean with

771 respect to silicate weathering – approximately one million years (Hain et al., 2018) such that net carbon
772 addition to or removal from the Earth System through volcanic outgassing or silicate weathering is
773 likely to be minor over the million-year timescale. However, during some short events, such as for
774 instance the Palaeocene-Eocene Thermal Maximum, considerable carbon was added to the system in
775 <200 kyr (e.g. Gutjahr et al., 2017) invalidating the formulation described in equation 2 on these
776 intervals. We also emphasize that this formalism is only valid as long as core sites remain in equilibrium
777 with the atmosphere.

778 4.4 Caveats and future studies.

779 The aim of this study is to evaluate the capacity of the $\delta^{11}\text{B}$ -pH proxy in *G. ruber* to accurately
780 reconstruct atmospheric CO_2 in the past. The overall agreement with the high confidence ice core CO_2
781 (e.g. Bereiter et al., 2015) is very promising and gives confidence to $\delta^{11}\text{B}$ -derived CO_2 reconstructions
782 beyond the ice core record (>800 ky). We have however identified occasional, minor offsets between
783 the two records and explored potential drivers (partial dissolution, $\delta^{11}\text{B}$ borate-foram calibration, local
784 air-sea disequilibrium). It is likely that the minor disagreement observed (Figure 5) has a combination
785 of drivers and that a single mechanism is not solely responsible for the CO_2 offsets observed. To confirm
786 these trends, we recommend future work to focus on the following:

787 (1) The improved $\delta^{11}\text{B}$ calibration approach should be tested at more core locations. We note that the
788 improved calibration to the ice core records reported here was achieved using data from two sites. While
789 care is taken in the choice of study site to minimize air-sea CO_2 disequilibrium and sediment dissolution,
790 the newly defined improved $\delta^{11}\text{B}_{\text{borate-foram}}$ calibration should be seen as an exercise that is tailored to the
791 available data in this study, and future high-resolution studies can apply the method used here (section
792 4.2.6 4.5) to further test how the *G. ruber* calibration changes if CO_2 offsets occur in a similar fashion
793 (i.e at a particular time in each glacial cycles). We note the importance of high resolution (at least 3 ky)
794 sampling in future studies because most CO_2 offsets observed are short lived.

795 (2) A multiproxy approach is ideally needed. In particular, reliable indicators of temperature and
796 productivity, to assess change in upwelling and foraminifera ecology. We encourage future studies to
797 expand high resolution boron-derived CO_2 record and ancillary data (C and O isotopes, proxy of
798 carbonate preservation and bottom water corrosiveness, biological productivity) to further constrain the
799 capacity of the boron isotope pH/ CO_2 proxy to generate reliable CO_2 records. As more recent IODP
800 expeditions include porewater data, constraints on bottom water conditions and degree of corrosiveness
801 at a given site will become available to evaluate the impact on $\delta^{11}\text{B}$ signals in foraminifera.

802 (3) Efforts should continue to decrease the analytical uncertainty associated with a $\delta^{11}\text{B}$ measurement
803 by MC-ICPMS because this still accounts for ~40% of the total uncertainty associated with each $\delta^{11}\text{B}$ -
804 derived CO_2 estimate.

805 (4) We find little evidence to suggest that partial dissolution of foraminiferal tests (*G. ruber*) is a major
806 driver of uncertainty in $\delta^{11}\text{B}$ -derived CO_2 estimates but ~~more well constrained thorough dissolution~~
807 experiments are desirable because of site-to-site differences in foraminifera taphonomy.
808

809 5. Conclusion.

810 We carried out the most thorough test to date of the $\delta^{11}\text{B}$ -pH (CO_2) proxy by comparing new high-
811 resolution (3 to 6 ky per sample) boron isotope-based pH and CO_2 at two locations with CO_2 from the
812 ice core record. Results suggest that the boron isotope proxy is robust and suited to reconstructing CO_2
813 to a precision of ± 46 ~~48~~ ppm (2σ , RMSE = ~~26~~ ~~25~~ ppm) over this interval, with little or no systematic
814 bias shown by a mean residual of ~~13~~ ~~±46~~ (~~2~~ ~~σ~~) ~~ppm~~ ~~4.6~~ ~~±49~~ (~~2~~ ~~σ~~) ~~ppm~~. This provides high confidence
815 to the application of the proxy beyond the reach of the ice core records.

816 Despite the overall good agreement, there are some minor short-lived CO₂ offsets that appear to have
817 some temporal structure and we explored a number of possible drivers. A visual correlation between
818 CO₂ offset and fragmentation index at core site 999 is observed (Figure 5) but is not statistically
819 significant. The effect of partial dissolution on $\delta^{11}\text{B}$ in *G. ruber* appears to be negligible in our record,
820 but the possible heterogeneity of $\delta^{11}\text{B}$ within shells as well as variable susceptibility to dissolution of the
821 different parts of the foraminifera, encourages further exploration.

822 A revised $\delta^{11}\text{B}$ borate–foram calibration was calculated by minimising the offset between $\delta^{11}\text{B}$ –
823 derived CO₂ and ice core CO₂ using published calibration (Henehan et al., 2013). While the new
824 calibration improves the fit to the ice core records, we caution against its use to estimate CO₂ given that
825 it is no longer independent of the ice core or the assumptions we make here to calculate CO₂ (i.e. that
826 TA is constant).

827 The formalism established by Hain et al. (2018) is robust, showing that relative CO₂ forcing in the past
828 can be determined from pH change alone, even in the face of significant uncertainty in $\delta^{11}\text{B}$ of seawater
829 and without the need to determine a second carbonate parameter. This will not only be of great interest
830 to determine CO₂ forcing in ancient geological times where $\delta^{11}\text{B}$ of seawater and a second carbonate
831 parameter are poorly constrained, but the nature of the observed relationship over the last 400 kyr
832 confirms that multiple drivers are likely responsible for glacial-interglacial CO₂ change.

833 **6. Data availability.**

834 All raw data ~~are will be~~ provided as supplementary information. ~~once the manuscript is accepted.~~

835

836 **7. Author contribution.**

837 E.d.l.V generated boron isotope and elemental data and wrote the manuscript. E.d.l.V, T.B.C, M.P.H
838 and G.L.F analysed the data. G.L.F, T.B.C, M.P.H and P.A.W contributed to the editing and
839 reviewing of the manuscript. M.W, R.G and D.C generated oxygen and carbon isotope data and
840 fragmentation index data. R.G and D.C were supervised by T.B.C and G.L.F. C.L assisted with
841 foraminifera picking and boron isotope analysis. E.d.l.V, T.B.C and G.L.F designed the research.

842

843 **8. Competing interest.**

844 The authors declare they have no conflict of interest.

845

846 **9. Acknowledgment.**

847 We warmly thank J. Andy Milton for assistance in MC-ICPMS and ICPMS analysis, and members of
848 the “B-team”, Agnes Michalik and Matthew Cooper for clean laboratory assistance. We thank
849 William Gray and one anonymous reviewer for insightful comments that improved the manuscript.
850 This work was funded by NERC grant NE/P011381/1 to GLF, PAW, TBC and MPH and by Royal
851 Society Wolfson Awards to both GLF and PAW.

852

853

854 **10. References.**

855

856 Ahn, J., et al. (2012). "Atmospheric CO₂ over the last 1000 years: A high-resolution record
857 from the West Antarctic Ice Sheet (WAIS) Divide ice core." Global Biogeochemical Cycles
858 **26**(2).

859

860 Anagnostou, E., et al. (2020). "Proxy evidence for state-dependence of climate sensitivity in
861 the Eocene greenhouse." Nature communications **11**(1): 1-9.

862

863 Anagnostou, E., et al. (2016). "Changing atmospheric CO₂ concentration was the primary
864 driver of early Cenozoic climate." Nature **533**(7603): 380-384.

865

866 Anagnostou, E., et al. (2019). "Calibration of the pH- $\delta^{11}\text{B}$ and temperature-Mg/Li proxies in
867 the long-lived high-latitude crustose coralline red alga *Clathromorphum compactum* via
868 controlled laboratory experiments." *Geochimica et Cosmochimica Acta* 254: 142-155.
869

870 Anand, P., et al. (2003). "Calibration of Mg/Ca thermometry in planktonic foraminifera from
871 a sediment trap time series." *Paleoceanography* 18(2).
872

873 [Anderson, R. F., et al. \(2019\). "Deep-sea oxygen depletion and ocean carbon sequestration
874 during the last ice age." *Global Biogeochemical Cycles* 33\(3\): 301-317.](#)
875

876

877 Aurahs, R., et al. (2011). "A revised taxonomic and phylogenetic concept for the planktonic
878 foraminifer species *Globigerinoides ruber* based on molecular and morphometric evidence."
879 *Marine Micropaleontology* 79(1-2): 1-14.
880

881 Barker, S., et al. (2006). "Globally increased pelagic carbonate production during the Mid-
882 Brunhes dissolution interval and the CO₂ paradox of MIS 11." *Quaternary Science Reviews*
883 25(23-24): 3278-3293.
884

885 Barker, S., et al. (2003). "A study of cleaning procedures used for foraminiferal Mg/Ca
886 paleothermometry." *Geochemistry, Geophysics, Geosystems* 4(9).
887

888 Bé, A. (1980). "Gametogenic calcification in a spinose planktonic foraminifer, *Globigerinoides*
889 *sacculifer* (Brady)." *Marine Micropaleontology* 5: 283-310.
890

891 Bé, A. W., et al. (1983). "Sequence of morphological and cytoplasmic changes during
892 gametogenesis in the planktonic foraminifer *Globigerinoides sacculifer* (Brady)." *Micropaleontology*: 310-325.
893

894

895 Bereiter, B., et al. (2015). "Revision of the EPICA Dome C CO₂ record from 800 to 600 kyr
896 before present." *Geophysical Research Letters* 42(2): 542-549.
897

898 Berger, W. H. (1970). "Planktonic foraminifera: selective solution and the lysocline." *Marine*
899 *Geology* 8(2): 111-138.
900

901 Boyle, E. A. (1988). "The role of vertical chemical fractionation in controlling late Quaternary
902 atmospheric carbon dioxide." *Journal of Geophysical Research: Oceans* 93(C12): 15701-
903 15714.
904

905 Boyle, E. A. (1988). "Vertical oceanic nutrient fractionation and glacial/interglacial
906 CO₂ cycles." *Nature* 331(6151): 55-56.
907

908 Brovkin, V., et al. (2007). "Lowering of glacial atmospheric CO₂ in response to changes in
909 oceanic circulation and marine biogeochemistry." *Paleoceanography* 22(4).
910

911 Brown, S. J. and H. Elderfield (1996). "Variations in Mg/Ca and Sr/Ca ratios of planktonic
912 foraminifera caused by postdepositional dissolution: Evidence of shallow Mg-dependent
913 dissolution." *Paleoceanography* 11(5): 543-551.
914

915 Caron, D. A., et al. (1990). "Effects of gametogenesis on test structure and dissolution of some
916 spinose planktonic foraminifera and implications for test preservation." Marine
917 Micropaleontology **16**(1-2): 93-116.

918

919 Cartapanis, O., et al. (2018). "Carbon burial in deep-sea sediment and implications for oceanic
920 inventories of carbon and alkalinity over the last glacial cycle." Climate of the Past **14**(11):
921 1819-1850.

922

923 Carter, A., et al. (2017). "Differing oxygen isotopic signals of two Globigerinoides ruber
924 (white) morphotypes in the East China Sea: Implications for paleoenvironmental
925 reconstructions." Marine Micropaleontology **131**: 1-9.

926

927 Chalk, T., et al. (2019). "Dynamic storage of glacial CO₂ in the Atlantic Ocean revealed by
928 boron [CO₃²⁻] and pH records." Earth and Planetary Science Letters **510**: 1-11.

929

930 Chalk, T. B., et al. (2017). "Causes of ice age intensification across the Mid-Pleistocene
931 Transition." Proceedings of the National Academy of Sciences **114**(50): 13114-13119.

932

933 [de Garidel-Thoron, T., et al. \(2005\). "Stable sea surface temperatures in the western Pacific](#)
934 [warm pool over the past 1.75 million years." Nature](#) **433**(7023): 294-298.

935

936

937 De La Vega, E., et al. (2020). "Atmospheric CO₂ during the Mid-Piacenzian Warm Period and
938 the M2 glaciation." Scientific reports **10**(1): 1-8.

939

940 Dekens, P. S., et al. (2002). "Core top calibration of Mg/Ca in tropical foraminifera: Refining
941 paleotemperature estimation." Geochemistry, Geophysics, Geosystems **3**(4): 1-29.

942

943 Dyez, K. A., et al. (2018). "Early Pleistocene obliquity-scale pCO₂ variability at~ 1.5 million
944 years ago." Paleoceanography and Paleoclimatology **33**(11): 1270-1291.

945

946 Dyez, K. A. and A. C. Ravelo (2013). "Late Pleistocene tropical Pacific temperature sensitivity
947 to radiative greenhouse gas forcing." Geology **41**(1): 23-26.

948

949 Dyez, K. A. and A. C. Ravelo (2014). "Dynamical changes in the tropical Pacific warm pool
950 and zonal SST gradient during the Pleistocene." Geophysical Research Letters **41**(21): 7626-
951 7633.

952

953 [Eggleston, S. and E. D. Galbraith \(2018\). "The devil's in the disequilibrium: multi-component](#)
954 [analysis of dissolved carbon and oxygen changes under a broad range of forcings in a general](#)
955 [circulation model." Biogeosciences](#) **15**(12): 3761-3777.

956

957

958 Farrell, J. W. and W. L. Prell (1989). "Climatic change and CaCO₃ preservation: An 800,000
959 year bathymetric reconstruction from the central equatorial Pacific Ocean." Paleoceanography
960 **4**(4): 447-466.

961

962 Fehrenbacher, J. S. and P. A. Martin (2014). "Exploring the dissolution effect on the intrashell
963 Mg/Ca variability of the planktic foraminifer Globigerinoides ruber." Paleoceanography **29**(9):
964 854-868.

965
966 Foster, G. (2008). "Seawater pH, pCO₂ and [CO₂- 3] variations in the Caribbean Sea over the
967 last 130 kyr: A boron isotope and B/Ca study of planktic foraminifera." Earth and Planetary
968 Science Letters **271**(1-4): 254-266.
969
970 Foster, G., et al. (2010). "Boron and magnesium isotopic composition of seawater."
971 Geochemistry, Geophysics, Geosystems **11**(8).
972
973 Foster, G. L., et al. (2012). "The evolution of pCO₂, ice volume and climate during the middle
974 Miocene." Earth and Planetary Science Letters **341**: 243-254.
975
976 Foster, G. L., et al. (2013). "Interlaboratory comparison of boron isotope analyses of boric acid,
977 seawater and marine CaCO₃ by MC-ICPMS and NTIMS." Chemical Geology **358**: 1-14.
978
979
980 Foster, G. L. and J. W. Rae (2016). "Reconstructing ocean pH with boron isotopes in
981 foraminifera." Annual Review of Earth and Planetary Sciences **44**: 207-237.
982
983
984 _____
985 _____
986 Gray, W. R. and D. Evans (2019). "Nonthermal influences on Mg/Ca in planktonic
987 foraminifera: A review of culture studies and application to the last glacial maximum."
988 Paleoceanography and Paleoclimatology **34**(3): 306-315.
989
990 Gray, W. R., et al. (2018). "The effects of temperature, salinity, and the carbonate system on
991 Mg/Ca in Globigerinoides ruber (white): A global sediment trap calibration." Earth and
992 Planetary Science Letters **482**: 607-620.
993
994
995 Greenop, R., et al. (2017). "A record of Neogene seawater δ¹¹B reconstructed from paired
996 δ¹¹B analyses on benthic and planktic foraminifera." Climate of the Past **13**(2): 149-170.
997
998 Guillermic, M., et al. (2022). "Atmospheric CO₂ estimates for the Miocene to Pleistocene
999 based on foraminiferal δ¹¹B at Ocean Drilling Program Sites 806 and 807 in the Western
1000 Equatorial Pacific." Climate of the Past **18**(2): 183-207.
1001
1002 Gutjahr, M., et al. (2017). "Very large release of mostly volcanic carbon during the Palaeocene–
1003 Eocene Thermal Maximum." Nature **548**(7669): 573-577.
1004
1005 Hain, M., et al. (2018). "Robust constraints on past CO₂ climate forcing from the boron isotope
1006 proxy." Paleoceanography and Paleoclimatology **33**(10): 1099-1115.
1007
1008 Hain, M. P., et al. (2014). "8.18–The biological Pump in the Past." Reference Module in Earth
1009 Systems and Environmental Sciences, Treatise on Geochemistry (Second Edition), The Oceans
1010 and Marine Geochemistry **8**: 485-517.
1011
1012

1013 Hain, M. P., et al. (2010). "Carbon dioxide effects of Antarctic stratification, North Atlantic
1014 Intermediate Water formation, and subantarctic nutrient drawdown during the last ice age:
1015 Diagnosis and synthesis in a geochemical box model." Global Biogeochemical Cycles **24**(4).
1016

1017 Hansen, J., et al. (2008). "Target atmospheric CO₂: Where should humanity aim?" arXiv
1018 preprint arXiv:0804.1126.
1019

1020 Harper, D., et al. (2020). "The magnitude of surface ocean acidification and carbon release
1021 during Eocene Thermal Maximum 2 (ETM-2) and the Paleocene-Eocene Thermal Maximum
1022 (PETM)." Paleoceanography and Paleoclimatology **35**(2): e2019PA003699.
1023

1024 Hemleben, C., et al. (1989). Modern Planktonic Foraminifera, Springer-Verlag.
1025

1026 Henehan, M. J., et al. (2016). "A new boron isotope-pH calibration for *Orbulina universa*, with
1027 implications for understanding and accounting for 'vital effects'." Earth and Planetary Science
1028 Letters **454**: 282-292.
1029

1030 Henehan, M. J., et al. (2015). "Evaluating the utility of B/C ratios in planktic foraminifera as
1031 a proxy for the carbonate system: A case study of *Globigerinoides ruber*." Geochemistry,
1032 Geophysics, Geosystems **16**(4): 1052-1069.
1033

1034 Henehan, M. J., et al. (2013). "Calibration of the boron isotope proxy in the planktonic
1035 foraminifera *Globigerinoides ruber* for use in palaeo-CO₂ reconstruction." Earth and Planetary
1036 Science Letters **364**: 111-122.
1037

1038 Henehan, M. J., et al. (2019). "Rapid ocean acidification and protracted Earth system recovery
1039 followed the end-Cretaceous Chicxulub impact." Proceedings of the National Academy of
1040 Sciences **116**(45): 22500-22504.
1041

1042 Hönisch, B., et al. (2003). "The influence of symbiont photosynthesis on the boron isotopic
1043 composition of foraminifera shells." Marine Micropaleontology **49**(1-2): 87-96.
1044

1045 Hönisch, B. and N. G. Hemming (2004). "Ground-truthing the boron isotope-paleo-pH proxy
1046 in planktonic foraminifera shells: Partial dissolution and shell size effects." Paleoceanography
1047 **19**(4).
1048

1049 Hönisch, B. and N. G. Hemming (2005). "Surface ocean pH response to variations in pCO₂
1050 through two full glacial cycles." Earth and Planetary Science Letters **236**(1-2): 305-314.
1051

1052 Hönisch, B., et al. (2009). "Atmospheric carbon dioxide concentration across the mid-
1053 Pleistocene transition." Science **324**(5934): 1551-1554.
1054

1055 Howard, W. R. and W. L. Prell (1994). "Late Quaternary CaCO₃ production and preservation
1056 in the Southern Ocean: Implications for oceanic and atmospheric carbon cycling." Paleoceanography **9**(3): 453-482.
1057

1058

1059 Iwasaki, S., et al. (2019). "Micro-CT Scanning of Tests of Three Planktic Foraminiferal Species
1060 to Clarify Dissolution Process and Progress." Geochemistry, Geophysics, Geosystems **20**(12):
1061 6051-6065.
1062

1063 John, S. G. and J. F. Adkins (2010). "Analysis of dissolved iron isotopes in seawater." Marine
1064 chemistry **119**(1-4): 65-76.

1065

1066 Johns, W. E., et al. (2002). "On the Atlantic inflow to the Caribbean Sea." Deep sea research
1067 part I: Oceanographic research papers **49**(2): 211-243.

1068

1069 Klochko, K., et al. (2006). "Experimental measurement of boron isotope fractionation in
1070 seawater." Earth and Planetary Science Letters **248**(1-2): 276-285.

1071

1072 Kohfeld, K. E. and A. Ridgwell (2009). "Glacial-interglacial variability in atmospheric CO₂."
1073 Surface ocean-lower atmosphere processes **187**: 251-286.

1074

1075 [Lauvset, S. K., et al. \(2022\). "GLODAPv2. 2022: the latest version of the global interior ocean](#)
1076 [biogeochemical data product." Earth System Science Data Discussions 2022: 1-37.](#)

1077

1078

1079 Lee, K., et al. (2010). "The universal ratio of boron to chlorinity for the North Pacific and North
1080 Atlantic oceans." Geochimica et Cosmochimica Acta **74**(6): 1801-1811.

1081

1082 Lemarchand, D., et al. (2002). "Boron isotope systematics in large rivers: implications for the
1083 marine boron budget and paleo-pH reconstruction over the Cenozoic." Chemical Geology
1084 **190**(1-4): 123-140.

1085

1086 Lisiecki, L. E. and M. E. Raymo (2005). "A Plio-Pleistocene stack of 57 globally distributed
1087 benthic $\delta^{18}\text{O}$ records." Paleoceanography **20**: 1-17.

1088

1089 Lombard1, F., et al. (2009). "Temperature effect on respiration and photosynthesis of the
1090 symbiont-bearing planktonic foraminifera *Globigerinoides ruber*, *Orbulina universa*, and
1091 *Globigerinella siphonifera*." Limnology and Oceanography **54**(1): 210-218.

1092

1093 Lueker, T. J., et al. (2000). "Ocean pCO₂ calculated from dissolved inorganic carbon,
1094 alkalinity, and equations for K₁ and K₂: validation based on laboratory measurements of CO₂
1095 in gas and seawater at equilibrium." Marine chemistry **70**(1-3): 105-119.

1096

1097 Lüthi, D., et al. (2008). "High-resolution carbon dioxide concentration record 650,000–800,000
1098 years before present." Nature **453**(7193): 379-382.

1099

1100 [Marchitto, T., et al. \(2014\). "Improved oxygen isotope temperature calibrations for](#)
1101 [cosmopolitan benthic foraminifera." Geochimica et Cosmochimica Acta 130: 1-11.](#)

1102

1103

1104 Martínez-Botí, M., et al. (2015). "Plio-Pleistocene climate sensitivity evaluated using high-
1105 resolution CO₂ records." Nature **518**(7537): 49.

1106

1107 Meilland, J., et al. (2021). "Population dynamics and reproduction strategies of planktonic
1108 foraminifera in the open ocean." Biogeosciences **18**(20): 5789-5809.

1109

1110 Ni, Y., et al. (2007). "A core top assessment of proxies for the ocean carbonate system in
1111 surface-dwelling foraminifers." Paleoceanography **22**(3).

1112

1113 Numberger, L., et al. (2009). "Habitats, abundance patterns and isotopic signals of
1114 morphotypes of the planktonic foraminifer *Globigerinoides ruber* (d'Orbigny) in the eastern
1115 Mediterranean Sea since the Marine Isotopic Stage 12." Marine Micropaleontology **73**(1-2):
1116 90-104.

1117
1118 Olsen, A., et al. (2016). "The Global Ocean Data Analysis Project version 2 (GLODAPv2)—an
1119 internally consistent data product for the world ocean." Earth System Science Data **8**(2): 297-
1120 323.

1121
1122 Olsen, A., et al. (2004). "Sea–air flux of CO₂ in the Caribbean Sea estimated using in situ and
1123 remote sensing data." Remote Sensing of Environment **89**(3): 309-325.

1124
1125 Oppo, D. and S. Lehman (1993). "Mid-depth circulation of the subpolar North Atlantic during
1126 the last glacial maximum." Science **259**(5098): 1148-1152.

1127
1128 Paillard, D., et al. (1996). "Macintosh program performs time-series analysis." Eos,
1129 Transactions American Geophysical Union **77**(39): 379-379.

1130
1131 Penman, D. E., et al. (2014). "Rapid and sustained surface ocean acidification during the
1132 Paleocene-Eocene Thermal Maximum." Paleoceanography **29**(5): 357-369.

1133
1134 Petit, J.-R., et al. (1999). "Climate and atmospheric history of the past 420,000 years from the
1135 Vostok ice core, Antarctica." Nature **399**(6735): 429-436.

1136
1137 Premoli-Silva, I. (1993). Shipboard Scientific Party, 1993a Site 871. Proc. ODP, Init. Repts.

1138
1139 Rae, J. W., et al. (2011). "Boron isotopes and B/Ca in benthic foraminifera: Proxies for the
1140 deep ocean carbonate system." Earth and Planetary Science Letters **302**(3-4): 403-413.

1141
1142 Raitzsch, M., et al. (2018). "Boron isotope-based seasonal paleo-pH reconstruction for the
1143 Southeast Atlantic—A multispecies approach using habitat preference of planktonic
1144 foraminifera." Earth and Planetary Science Letters **487**: 138-150.

1145
1146 [Rebotim, A., et al. \(2017\). "Factors controlling the depth habitat of planktonic foraminifera in
1147 the subtropical eastern North Atlantic." Biogeosciences **14**\(4\): 827-859.](#)

1148
1149 Rohling, E., et al. (2013). "Making sense of palaeoclimate sensitivity (vol 491, pg 683, 2012)."
1150 Nature **494**(7435): 130-130.

1151
1152 Rohling, E. J., et al. (2018). "Comparing climate sensitivity, past and present." Annual Review
1153 of Marine Science **10**: 261-288.

1154
1155
1156 Sadekov, A. Y., et al. (2010). "Effects of seafloor and laboratory dissolution on the Mg/Ca
1157 composition of *Globigerinoides sacculifer* and *Orbulina universa* tests—A laser ablation
1158 ICPMS microanalysis perspective." Earth and Planetary Science Letters **292**(3-4): 312-324.

1159
1160 Sanyal, A., et al. (1995). "Evidence for a higher pH in the glacial ocean from boron isotopes in
1161 foraminifera." Nature **373**(6511): 234-236.

1162

1163 Schlitzer, R. (2022). "Ocean data view."
1164
1165 Schmidt, M. W., et al. (2006). "Western Caribbean sea surface temperatures during the late
1166 Quaternary." Geochemistry, Geophysics, Geosystems **7**(2).
1167
1168 Seki, O., et al. (2010). "Alkenone and boron-based Pliocene pCO₂ records." Earth and
1169 Planetary Science Letters **292**(1-2): 201-211.
1170
1171 Sexton, P. F. and S. Barker (2012). "Onset of 'Pacific-style' deep-sea sedimentary carbonate
1172 cycles at the mid-Pleistocene transition." Earth and Planetary Science Letters **321**: 81-94.
1173
1174 Siegenthaler, U., et al. (2005). "Stable carbon cycle climate relationship during the Late
1175 Pleistocene." Science **310**(5752): 1313-1317.
1176
1177 Sigman, D. M., et al. (2021). "The Southern Ocean during the ice ages: A review of the
1178 Antarctic surface isolation hypothesis, with comparison to the North Pacific." Quaternary
1179 Science Reviews **254**: 106732.
1180
1181 Sigman, D. M., et al. (2010). "The polar ocean and glacial cycles in atmospheric CO₂
1182 concentration." Nature **466**(7302): 47-55.
1183
1184
1185 Sigman, D. M., et al. (1998). "The calcite lysocline as a constraint on glacial/interglacial low-
1186 latitude production changes." Global Biogeochemical Cycles **12**(3): 409-427.
1187
1188 Spero, H. J., et al. (1997). "Effect of seawater carbonate concentration on foraminiferal carbon
1189 and oxygen isotopes." Nature **390**(6659): 497-500.
1190
1191 Steinke, S., et al. (2005). "Mg/Ca ratios of two *Globigerinoides ruber* (white) morphotypes:
1192 Implications for reconstructing past tropical/subtropical surface water conditions." Geochemistry, Geophysics, Geosystems **6**(11).
1193
1194
1195 Takagi, H., et al. (2019). "Characterizing photosymbiosis in modern planktonic foraminifera." Biogeosciences **16**(17): 3377-3396.
1196
1197
1198 Takahashi, T., et al. (2009). "Climatological mean and decadal change in surface ocean pCO₂,
1199 and net sea-air CO₂ flux over the global oceans." Deep Sea Research Part II: Topical Studies
1200 in Oceanography **56**(8-10): 554-577.
1201
1202 Toggweiler, J. (1999). "Variation of atmospheric CO₂ by ventilation of the ocean's deepest
1203 water." Paleoceanography **14**(5): 571-588.
1204
1205 Wang, L. (2000). "Isotopic signals in two morphotypes of *Globigerinoides ruber* (white) from
1206 the South China Sea: implications for monsoon climate change during the last glacial cycle." Palaeogeography, Palaeoclimatology, Palaeoecology **161**(3-4): 381-394.
1207
1208
1209 Wycech, J. B., et al. (2018). "Combined effects of gametogenic calcification and dissolution
1210 on $\delta^{18}\text{O}$ measurements of the planktic foraminifer *Trilobatus sacculifer*." Geochemistry,
1211 Geophysics, Geosystems **19**(11): 4487-4501.
1212

1213 York, D., et al. (2004). "Unified equations for the slope, intercept, and standard errors of the
1214 best straight line." American journal of physics **72**(3): 367-375.

1215

1216 Zeebe, R. E. and D. Wolf-Gladrow (2001). CO₂ in seawater: equilibrium, kinetics, isotopes,
1217 Gulf Professional Publishing.

1218

1219 Zeebe, R. E., et al. (2003). "Vital effects in foraminifera do not compromise the use of $\delta^{11}\text{B}$
1220 as a paleo-pH indicator: Evidence from modeling." Paleoceanography **18**(2).

1221

1222

1223